

# The Upgraded DØ Detector

names

(DØ Collaboration)

institutions

---

## Abstract

The DØ experiment enjoyed a very successful data-collection run at the Fermilab Tevatron collider between 1992 and 1996. Since then, the detector has been upgraded to take advantage of improvements to the Tevatron and enhance its physics capabilities. We describe the design and performance of the new aspects of the detector, including the silicon microstrip tracker, scintillating-fiber tracker, solenoidal magnet, preshower detector, forward muon detector, and forward proton detector. The associated electronics, triggering and data acquisition systems are also presented, along with the design and implementation of software which is specific to DØ.

---

## 1 Introduction

The DØ experiment was proposed in 1982 to study proton-antiproton collisions at  $\sqrt{s} = 1.8$  TeV at the Fermilab Tevatron collider. The focus of the experiment was the study of high mass states and large  $p_T$  phenomena. The detector performed very well during Run I of the Tevatron, 1992–1996, leading to the discovery of the top quark [1], a precision measurement of the mass of the  $W$  boson [2], detailed analysis of gauge boson couplings [3], and greatly improved limits on the production of new phenomena such as leptoquarks [4,5] and supersymmetric particles [6], among many other accomplishments [7].

During Run I, the Tevatron contained six bunches each of protons and antiprotons, with 3500 ns between bunch crossings and a center of mass energy of 1.8 TeV. The instantaneous luminosity was about  $1\text{--}2 \times 10^{31} \text{ cm}^{-2}\text{s}^{-1}$  and approximately  $120 \text{ pb}^{-1}$  of data were recorded by DØ. The Tevatron has been upgraded to 36 bunches of protons and antiprotons with a bunch spacing of 396 ns which will be reduced to 132 ns with approximately 100 bunches in

the future. The instantaneous luminosity will increase a factor of ten to  $1\text{--}2 \times 10^{32} \text{ cm}^{-2}\text{s}^{-1}$  and more than  $2 \text{ fb}^{-1}$  of data is expected to be recorded. In addition, the center of mass energy has risen to 1.96 TeV.

To take advantage of these improvements in the Tevatron and to enhance the physics reach of the experiment, we have significantly upgraded the DØ detector. The detector consists of three major subsystems: central tracking detectors, uranium/liquid-argon calorimeters, and a muon spectrometer. The original DØ detector and data acquisition system are described in detail in Ref. [8]. The central tracking system has been completely replaced; the old system suffered from radiation damage and improved tracking technologies are now available. The new system includes a silicon microstrip tracker and a scintillating-fiber tracker located within a 2 T solenoidal magnet. The silicon microstrip tracker is able to identify displaced vertices for  $b$ -quark tagging; the magnetic field provides  $E/p$  measurements for electron identification and calorimeter calibration, and allows us to identify low- $p_T$  muons. Between the solenoidal magnet and the central calorimeter and in front of the forward calorimeters, preshower detectors have been added for additional electron identification. The forward muon proportional drift chambers have been replaced by mini-drift tubes and trigger scintillation counters which can withstand the harsh radiation environment and additional shielding has been added. We have also added a forward proton detector for the study of diffractive physics. A side view of the upgraded DØ detector is shown in Figure 1.

The large reduction in the bunch spacing demanded the improvement of the read-out electronics and the implementation of pipelining for the front-end signals from the tracking, calorimeter and muon systems. The calorimeter preamplifiers and signal-shaping electronics have been replaced, as have all of the electronics for the muon system. A new trigger level has been added to reduce the event rate along with trigger hardware to identify displaced secondary vertices for  $b$ -quark tagging. Muon triggering has been enhanced by the addition of central and forward scintillation counters.

A significant improvement to the detector was the removal of the old main ring beam pipe from the calorimeters. During Run I, the main ring was used to accelerate protons for antiproton production while the Tevatron operated in collider mode. Losses from the main ring produced spurious energy depositions in the calorimeters and most triggers were not accepted while protons passed through the detector. Removal of the main ring increased the livetime of the detector by approximately 10%, depending on the trigger.

In the following sections of this paper, we describe the design and performance of the upgraded DØ detector. The new central tracking system and solenoidal magnet are presented in Sections 2 and 3, respectively. The preshower detectors are described in Section 4. The calorimeters are briefly described in

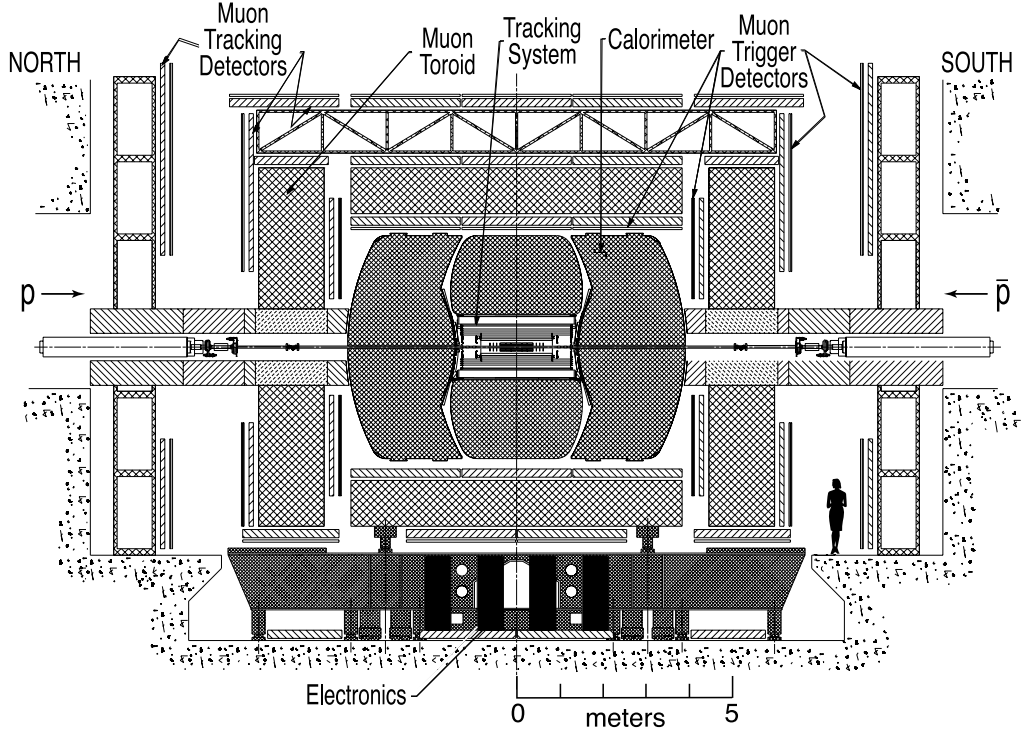


Fig. 1. Side view of the upgraded DØ detector.

Section 5 along with the new calorimeter electronics. The muon system is discussed in Section 7. The new forward proton detector is presented in Section 8. The triggering and data acquisition systems are described in Section 10. Detector services and an overview of the software components of the experiment are covered in Sections 11 and 12.

We use a right-handed coordinate system in which the  $z$ -axis is along the proton direction and the  $y$ -axis is upward. The angles  $\phi$  and  $\theta$  are the azimuthal and polar angles ( $\theta = 0$  along the proton beam direction), respectively. The  $r$  coordinate denotes the perpendicular distance from the  $z$  axis. The pseudorapidity,  $\eta = -\ln[\tan(\theta/2)]$ , approximates the true rapidity,  $y = 1/2 \ln[(E + p_z c)/(E - p_z c)]$ , for finite angles in the limit that  $(mc^2/E) \rightarrow 0$ .

## 2 Central tracking

Excellent tracking in the central region is necessary for our studies of top quark and electroweak physics and to search for new phenomena, including the Higgs boson. The central tracking system consists of a silicon vertex detector and the central fiber tracker surrounded by a solenoidal magnet. Working together, the two detectors locate the primary interaction vertex with a resolution of

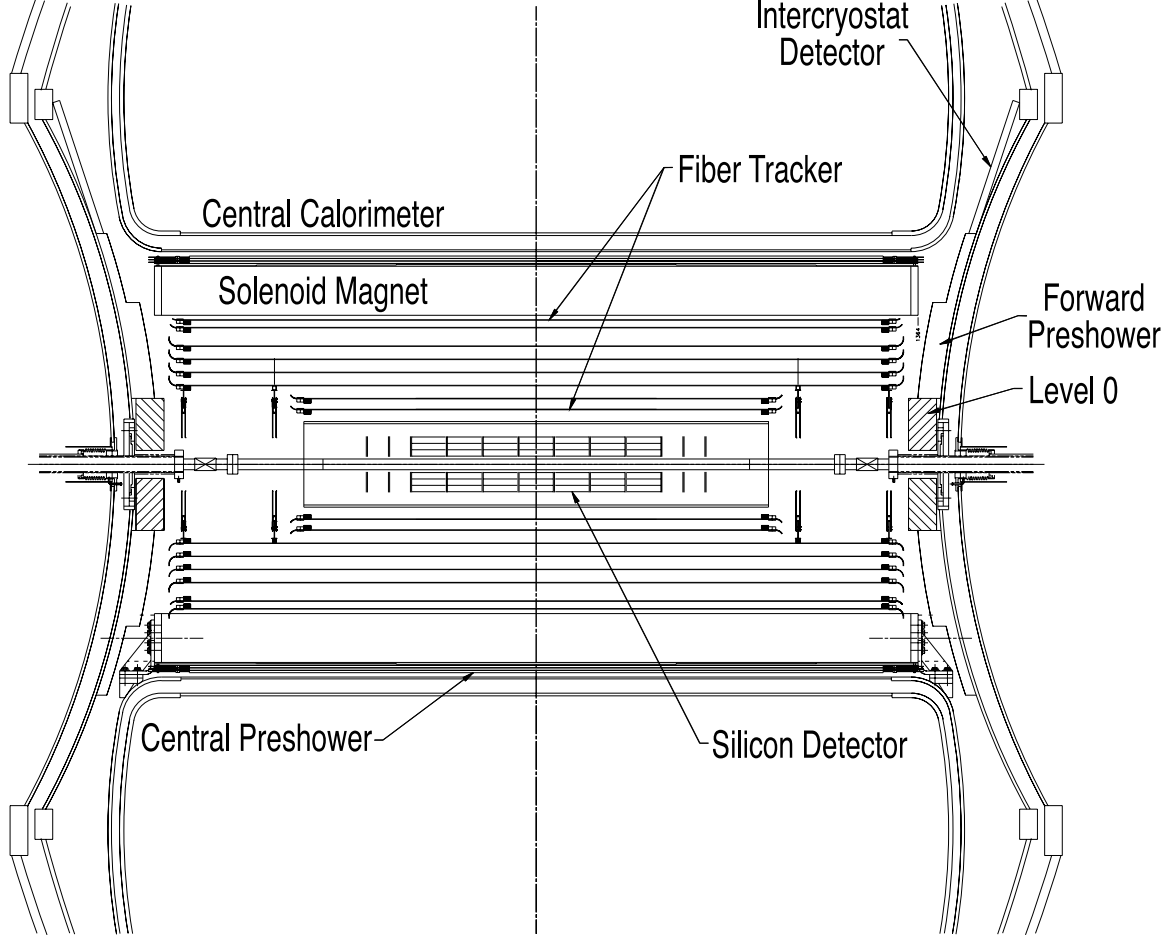


Fig. 2. The new central tracking system. Also shown are the location of the solenoid and the central preshower detector.

about  $35 \mu\text{m}$  along the beamline. They can tag  $b$  quark jets with an impact parameter resolution less than  $15 \mu\text{m}$  in  $r - \phi$  for particles with  $p_T > 10 \text{ GeV}/c$  at  $|\eta| = 0$ . The high resolution of the vertex position allows good measurement of lepton  $p_T$ , jet  $E_T$ , and  $\cancel{E}_T$ . Calibration of the electromagnetic calorimeter using the  $E/p$  ratio of electrons is now possible.

Both the SMT and CFT provide tracking information for the trigger. The CFT has two readouts for triggering: a fast and continuous readout of discriminator signals to the Level 1 trigger system and a slower readout of both the fast discriminator signals and digitized analog signals to the Level 2 and 3 systems. The SMT provides ??? to the Level 2 and 3 trigger systems and is used to trigger on displaced vertices from  $b$ -quark decay.

A schematic view of the central tracking system is shown in Figure 2.

## 2.1 Silicon microstrip tracker

### 2.1.1 SVXIIe readout system

## 2.2 Central Fiber Tracker

The Central Fiber Tracker (CFT) consists of scintillating fibers mounted on eight concentric support cylinders and occupies the radial space from 20 to 52 cm from the center of the beampipe. The two innermost cylinders are 1.66 m long; the outer six cylinders are 2.52 m long. Each cylinder supports one doublet layer of fibers oriented along the beam direction ( $z$ ) and a second doublet layer at a stereo angle of  $+3^\circ$  ( $u$ ) or  $-3^\circ$  ( $v$ ). Doublet layers with fibers oriented along the beam axis are referred to as axial layers, while the doublet layers oriented at small angles are referred to as stereo layers. From the smallest cylinder outward, the fiber orientation is  $zu - zv - zu - zv - zu - zv - zu - zv$ . The scintillating fibers are coupled to clear fiber waveguides which pipe the scintillation light to visible light photon counters (VLPCs) for read out. Scintillating fiber detectors are discussed in detail in Ref. [9].

Signals from the axial doublet layers are used to form a fast Level 1 hardware trigger based upon the number of track candidates above a specified  $p_T$  threshold (with a minimum threshold of 1.5 GeV/ $c$ ). Signals from all fibers are processed on a Level 1 trigger accept, and are used as input to the higher level triggers.

### 2.2.1 Fibers

The scintillating fibers, including cladding, are 835  $\mu\text{m}$  in diameter and 1.66 or 2.52 m in length. They are optically connected to clear fiber waveguides of identical diameter which are 7.8 to 11.9 m long. The fibers were manufactured by Kuraray [10] and have a multi-clad structure consisting of a core surrounded by two claddings. The scintillating fiber is structurally and chemically similar to the clear fiber, but contains fluorescent dyes. The CFT uses about 200 km of scintillating fiber and 800 km of clear fiber.

Light production in the fibers is a multistep process. The base core material is polystyrene (PS). The PS is doped with the organic fluorescent dye paraterphenyl (PTP), about 1% by weight. Excitations in the PS are rapidly transferred to the PTP via a non-radiative dipole-dipole interaction. PTP has a rapid fluorescence decay (a few nanoseconds) and a short emission wavelength ( $\approx 340$  nm). The mean free path of the emitted light is only a few hundred microns in the PS. To get the light out of the detector, a secondary, or wave-shifter, dye, 3-hydroxyflavone (3HF), is added at a low concentration

Fig. 3. Technique for curved scintillating fiber ribbon fabrication.

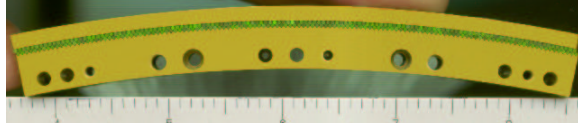


Fig. 4. A CFT fiber ribbon mass terminated via a v-groove connector.

(1500 ppm). The 3HF is spectrally matched to the PTP but has minimal optical self-absorption. The 3HF absorbs the 340 nm radiation from the PTP and re-emits it at 530 nm which is well-transmitted in PS.

Surrounding the PS core, whose refractive index is  $n = 1.59$ , are two claddings, each  $\approx 25 \mu\text{m}$  thick: an inner layer of polymethylmethacrylate (PMMA) with  $n = 1.49$ , and an outer layer of fluoro-acrylic with  $n = 1.42$ . The PMMA inner cladding serves as a mechanical interface between the core and the outer cladding, which are mechanically incompatible. The multicladd fiber is both mechanically and optically superior to single-clad fiber and typical values of the attenuation length are  $\approx 5 \text{ m}$  for the scintillating fiber and  $\approx 8 \text{ m}$  for the clear fiber.

We observe the light from only one end of each scintillating fiber. The opposite end of each of the scintillating fibers is mirrored by sputtering with an aluminum coating that provides a reflectivity of 85 to 90%.

The scintillating fibers were made into ribbons consisting of 256 fibers in two layers of 128 fibers each. Precisely spaced grooves were machined into a long,  $1/16''$ -thick piece of Delrin plastic. The spacing between the grooves varies between 919 and 965  $\mu\text{m}$  and depends on the radius of the corresponding support cylinder. The grooved plastic was inserted into a rigid, curved backing with the desired radius and the scintillating fibers were laid in and glued together to form the doublet ribbons; the two layers of fiber are offset by one-half of the fiber spacing. The technique is illustrated in Figure 3 and creates curved ribbons to match the curvature of each support cylinder without machining precisely-spaced grooves into a curved surface. Details on fiber lengths and spacing are provided in Table 1.

The read-out ends of the fibers are carefully positioned and adhesively bonded into v-groove connectors, and then the mass terminated ribbon and connector are polished to facilitate high efficiency light transmission across the connector joint. A polished curved connector is shown in Figure 4. Each 256-fiber waveguide bundle terminates in a matching curved connector. The connectors for each doublet fiber layer are different since the connectors must have the correct curvature for each layer. The light transmission through the v-groove connectors, with optical grease between the fiber ends, is  $\approx 95\%$ .

Table 1  
Design parameters of the CFT

Layer	Radius (cm)	Fibers/Sector	Fibers/Layer	Fiber separation ( $\mu\text{m}$ )	Active Length (m)
A	19.99	16	$1280 \times 2$	979.3	1.66
<i>Au</i>	20.15	16	$1280 \times 2$	987.2	1.66
B	24.90	20	$1600 \times 2$	975.8	1.66
<i>Bv</i>	25.60	20	$1600 \times 2$	982.1	1.66
C	29.80	24	$1920 \times 2$	973.4	2.52
<i>Cu</i>	29.97	24	$1920 \times 2$	978.6	2.52
D	34.71	28	$2240 \times 2$	971.7	2.52
<i>Dv</i>	34.87	28	$2240 \times 2$	976.2	2.52
E	39.62	32	$2560 \times 2$	970.4	2.52
<i>Eu</i>	39.78	32	$2560 \times 2$	974.4	2.52
F	44.53	36	$2880 \times 2$	969.5	2.52
<i>Fv</i>	44.69	36	$2880 \times 2$	972.9	2.52
G	49.43	40	$3200 \times 2$	968.7	2.52
<i>Gu</i>	49.59	40	$3200 \times 2$	971.8	2.52
H	51.43	44	$3520 \times 2$	916.1	2.52
<i>Hv</i>	51.59	44	$3520 \times 2$	919.0	2.52

After the fiber ribbons were fabricated, a  $^{57}\text{Co}$  x-ray source was used to verify the accuracy of the fiber placement and the responses of the fibers and transmission efficiency of the connectors for the ribbons. The position of each fiber within a ribbon was verified with an accuracy of better than  $25 \mu\text{m}$  rms.

### 2.2.2 Mechanical support structure

The eight support cylinders are each double-walled with a core of Rohacell. The walls are constructed from linear carbon fibers impregnated with about 40% resin. To minimize sagging of the cylinders, the carbon fibers were applied in layers in the following pattern:  $0^\circ/60^\circ/-60^\circ/\text{core}/-60^\circ/60^\circ/0^\circ$  where the numbers are the angles in degrees of the carbon fibers with respect to the axis of the cylinder. Each carbon fiber layer is about 0.0025" thick; the total thickness of carbon per cylinder is 0.016". After fabrication, the outside diameters of the cylinders were measured and compared to a perfect cylinder. The average (maximum???) deviation is ????

The requirements of the Level 1 hardware trigger constrain the design of the

CFT, particularly in the placement of the scintillating fiber ribbons. Offline reconstruction of the CFT data can incorporate corrections for misalignment of fibers, but that is not possible in the hardware trigger. So, the axial fibers had to be placed on the support cylinders such that any skew away from parallel to the beam axis is less than  $40\text{ }\mu\text{m}$  from end to end. Consequently, the individual fiber ribbons were precisely positioned and bonded to the outer surface of each cylinder prior to nesting the cylinders. ???Global placement precision was 33 micron for axial layers?? The connectors for the axial ribbons are all on one end of the cylinder, while the connectors for the corresponding stereo ribbons are all on the opposite end of the cylinder.

Successive cylinders are interlocked together by thin carbon-fiber annular rings which connect the inner surface of one cylinder's end ring to a flange mounted on the outer surface of the cylinder immediately inside. (??? This is not clear. How is this done without blocking the scintillating fibers???) The fiber connectors and connecting rings seal the fiber volume.

For a track traversing the detector at normal incidence, the total thickness of the fiber ribbons is 0.05 radiation lengths. The mechanical support structure contributes only 0.04 radiation lengths, but is very strong and rigid so that the fiber position will remain stable over the life of the experiment.

### 2.2.3 Waveguides

The clear fiber waveguides range in length from 7.8 to 11.9 m, and use the clear fibers described in Section 2.2.1. The waveguides generally contain 256 clear fibers inside a flexible protective plastic light shield. One end is mass terminated in a curved Delrin connector machined to mate to the corresponding connector at the end of the scintillating fiber ribbon. The mass terminated curved connector end is polished using a diamond fly cutter. About 40 cm from the other end of the waveguide, the 256 fibers are then separated in  $\phi$  into two groups of 128 fibers. Each group is covered with a flexible plastic protective light shield. These fibers are individually routed into the appropriate locations in two rectangular connectors that are designed to mate to the VLPC cassettes (described in Section 2.2.4). These molded plastic rectangular connectors are composed of Noryl N190 [11] with Celogen RA foam [12] to minimize distortions. After the fibers are potted into the rectangular connectors, the rectangular connectors are polished and the routing of the fibers is verified.

The clear fiber waveguides are routed from the ends of the CFT to the VLPCs located  $\approx 6$  m below the central calorimeter cryostat through the small gaps between the central and end calorimeter cryostats. These gaps also contain the forward preshower detectors (Section 4.3) and their waveguide fibers. The nar-



rowest region, between a forward preshower detector and the solenoidal magnet, is 1.5" wide. The bundles are routed on the face of the central calorimeter cryostat so that their ends are approximately aligned at the VLPC cassettes. The waveguides follow complex paths along the central calorimeter cryostat to minimize their depth in  $z$  and provide the proper timing at the VLPCs. The waveguide routing is illustrated in Figure 5.

#### *2.2.4 Visible light photon counter cassettes*

The light generated by the passage of charged particles through the scintillating fibers of the CFT is converted into electrical signals by the visible light photon counters (VLPC) housed in the VLPC cassettes. VLPCs are impurity-band silicon avalanche photodetectors which operate at 9 K, and are capable of detecting single photons [13,14]. They provide fast response, excellent quantum efficiency ( $\geq 75\%$ ), high gain (17,000 to 65,000), low gain dispersion and the capability of functioning in a high background environment. For an instantaneous luminosity of  $2 \times 10^{32} \text{ cm}^{-2}\text{s}^{-1}$ , the fiber-doublet hit efficiency is expected to be above 98%.

VLPCs are fabricated by growing a series of doped and undoped silicon layers on silicon substrate wafers using standard processing techniques. Individual wafers yield a maximum of 176 VLPC chips after dicing, and each chip contains a two by four array of 1 mm diameter pixels. Each eight-pixel chip is soldered to an aluminum nitride substrate, and the outputs from individual pixels are wirebonded to individual contact pads on the substrate. Non-uniformities in the VLPC production process result in variations in the VLPC characteristics such as gain, quantum efficiency, and thermal noise rates among and across VLPC wafers [15]. Due to these variations, the bias voltage at which the VLPCs operate at optimal signal-to-noise ratio varies between 6 and 8 volts. To reduce the complexity of the bias voltage and threshold implementations in the read-out electronics, the VLPC chips are carefully sorted and assigned to specific cassettes to allow for optimal performance.

VLPC cassettes mounted in cryostat slots provide the mechanical support, optical alignment, and appropriate operating environment for the VLPCs. Figure 6 shows an outside view of a cassette with a readout board attached. Each VLPC cassette houses 128 VLPC chips, and thus provides 1024 individual pixels of light-sensitive detector. (Details on the specially-designed VLPC cryostats are available elsewhere [16].) Cassettes are approximately 88 cm tall, 48 cm wide, and 4.4 cm thick. Individual 0.965 mm diameter fibers inside each cassette guide light from the clear fiber waveguides to individual VLPC pixels, and flex circuits provide paths for the electrical signals from the VLPCs to the pre-amplifiers on the analog front end boards (AFEs) which are mounted on the cassette body. In addition to pre-amplifiers, the AFEs also provide trig-

ger discrimination, temperature control, and bias-voltage control electronics. Details on the AFEs are provided in Section 2.2.5.

Each VLPC cassette consists of a cassette body housing eight modules. A view of the internal structure of a partially assembled cassette is shown in Figure 7. Each module is composed of a 128-fiber bundle and a cold-end assembly. The cassettes are designed so that modules can be readily extracted to allow repair of the cold-end assemblies. The 128-fiber bundle terminates at the top end in a rectangular molded optical connector (referred to as the warm-end optical connector), and at the bottom (cold) end in sixteen groups of eight fibers. The ends of the fibers are polished and each group of eight fibers is glued into a molded plug. The plugs (and mating boxes) are precision molded parts made of carbon fiber loaded polyphenylene sulfide (PPS) plastic. A polyurethane feedthrough block is cast around the 128 fibers and the flex circuits to form the barrier between the warm and the cold ends of the cassette. The fibers accept light from the clear fiber waveguides which are connected to the warm-end optical connectors at the top of the cassette and pipe the light to the VLPCs mounted in the cold-end assemblies.

The cold-end assembly hangs from the PPS plugs and consists of sixteen 8-channel VLPC hybrid assemblies supported on an isotherm. The inset in the lower left corner of Figure 6 shows a view of a cold-end assembly supported on a 128-fiber bundle, and Figure 8 shows an exploded view of the components of a cold-end assembly.

A VLPC hybrid assembly is composed of a PPS box adhesively bonded to the aluminum nitride substrate upon which a VLPC chip is mounted. The molded PPS box is precisely positioned (maintaining  $25\text{ }\mu\text{m}$  tolerances) so that the eight polished fibers in the PPS plug will be aligned over the individual VLPC pixels when the plug and box are mated, thus achieving good light collection efficiency while minimizing optical crosstalk between neighboring channels. Connectors are clamped across the contact pads on the aluminum nitride substrates and mated to flex circuits which transmit single-ended electrical signals between the cold-end and the AFE. Each module contains two flex circuits, and these flexible printed circuits are realized on  $5\text{ }\mu\text{m}$  thick adhesiveless copper coatings on a  $51\text{ }\mu\text{m}$  thick polyimide base material. The individual traces are  $76\text{ }\mu\text{m}$  wide with minimum  $89\text{ }\mu\text{m}$  spacings between circuit features. Each flex circuit is  $41.1\text{ cm}$  long. The isotherm also supports a calibrated carbon resistor that serves as a temperature sensor and resistors used as heaters, as well as the required springs and fasteners. The temperature sensor and heaters are employed to control the temperature of the VLPCs to within  $100\text{ mK}$ .

The cassette body can be viewed as composed of cold-end and warm-end mechanical structures. The cold-end structure (that portion of the cassette that is inserted in the cryostat) is composed of several sub-assemblies: the

feedthrough assembly, the G-10 side walls, the heat intercept assemblies, and the cold-end copper cup. The cassette is mounted to the top plate of the cryostat at the feedthrough assembly. This assembly provides the gas-tight seal for the cold,  $\leq 2$  psig, stagnant helium gas volume within the cryostat. Side walls composed of G-10 support the top (or liquid nitrogen) intercept which serves to cut off the flow of heat from the warm end. Another set of G-10 side walls support the bottom (or liquid helium) intercept. The bottom intercept supports the copper cup which surrounds the isotherms at the ends of the modules.

The warm-end structure is made of parallel tin-plated aluminum panels separated by spacer bars that form a protective box for the optical fibers. Rails mounted on the aluminum panels support the two AFEs. The warm-end Cin::apse [17] connector assembly enables the connection between the flex circuits and the AFEs. The AFEs mate to backplane connectors mounted on a backplane support structure via card edge connectors. The backplane support structures are bolted to the VLPC cryostats, and thus the combination of cassettes and cryostat serve as the crates for the AFEs that are mounted on the cassettes. Note that this design (with connections on two orthogonal edges of the AFE) allows the AFEs to be removed for service without extracting the cassette from the cryostat.

The CFT requires 76,800 channels of VLPC readout, and the central and forward preshower detectors are instrumented with an additional 22,564 channels of VLPC readout. The 99 cassettes necessary to provide this readout are mounted in the two custom-designed cryostats located on the platform beneath the DØ detector. Better than 99.8% of the individual VLPC channels in these cassettes were determined to meet or exceed the desired performance specifications during cryogenic qualification tests performed prior to installation at DØ.

### *2.2.5 CFT Read-out electronics*

The Central Fiber Tracker, the central preshower detector, and the forward preshower detector all share a VLPC-based readout and similar Level 1 and Level 2 trigger electronics, and therefore all three use the same front end electronics to process the signals from the VLPCs. The front end electronics are custom printed circuit boards approximately 14" tall (9U) and 18" long which are mounted on the VLPC cassettes inserted into cryostats as described in Section 2.2.4. These boards are referred to as analog front end boards, or AFEs.

The AFE is a large and complex board that must perform a number of functions with competing requirements. It has charge sensitive amplifiers to deal

with the very small signals from the VLPCs. It is part of the Level 3 readout, part of the Level 1 trigger, and part of the slow control and monitoring system. It must also control the bias and temperature of the VLPCs. (This functionality must be embedded in the AFE because it is the only electronics that interfaces to the VLPCs.) It must serve three different sub-detectors with different dynamic range requirements and comes in two types — left handed and right handed, depending on which side of the cassette body the board is mounted.

A number of features make it possible for the AFE to fulfill all of the above requirements. First, only a single printed circuit board was designed and laid out. The “handedness” of the board is determined by the way a very few key components are installed. So, for example, there are mounting points and traces for the hard metric connectors on both ends of the board. When the connector is mounted on one end of the board, the board becomes left handed and mounts on the left side of the cassette. When the connector is mounted on the other end of the board, the AFE is right handed. The great majority of the components are mounted exactly the same way on both left and right handed AFEs. Second, the most noise sensitive parts of the board, including the front end amplifier chips, are mounted on separate multi-chip modules (MCMs), each with its own regulator for the power and separate ground planes. The amplifier chips are wire bonded directly to these much smaller (3.5” by 1.5”) subassemblies. This allows the very fine pitch required for wire bonding to be confined to only the MCM substrate. Otherwise the AFE boards would not be manufacturable. This also allows the MCM subassemblies to be tested separately from the AFEs and to be removed as required for repair or replacement. There are eight MCMs on the AFE, each serving 64 VLPC channels, to match the construction of the cassette modules as described in Section 2.2.4. The MCMs are intended to be identical. To accommodate the different dynamic ranges of the CFT, the central preshower detector, and the forward preshower detector, capacitive charge division is used. By properly sizing the AC coupling capacitors on the AFE, the charge seen by the amplifiers is adjusted to accommodate the required dynamic range with the same electronics.

To further reduce the cost and simplify the system, the front end amplifier and digitizer is the same chip used for the DØ silicon microstrip tracker. This also facilitates commonality further downstream in the readout chain. The SVXIIe and its readout are described in detail in Section 2.1.1. On the AFE, the SVXIIe provides for the integration of the charge signals from the VLPCs, a pipeline for storing the signals while the trigger is formed, and digitization of the signals and sparsification of the digitized data for readout. There are eight SVXIIe chips on every AFE, one on each MCM. The SVXIIe chips share a single 8-bit bus for readout. However, because the signals from the AFE are also needed for the trigger system, another chip, the SIFT chip, provides a trigger pickoff. A simplified schematic is shown in Figure 9. Each SIFT chip has

eighteen channels so there are four SIFT chips on every MCM (eight channels are unused). The SIFT chips receive the signals from the VLPCs before the SVXIIe. For each channel, the SIFT has a preamplifier which integrates the incoming charge and switched capacitors which are used to split the amplified signal and send it along two paths: one, to the SVX, for later digitization and readout, the other to present the signal to a discriminator which fires if the charge exceeds some preset threshold (typically 10 to 15 fC). Figure 10 shows a photograph of part of an MCM.

There are five clock signals that control the operation of the SIFT, as can be seen from the schematic. One is the reset of the integrator, PRST, another is the reset for the discriminator, DRST. The third, SH (sample and hold) samples the discriminator output and the analog value of the integrator at the end of the cycle. READ transfers the analog charge to the SVXIIe. PCLMP resets the bias for the followers in the analog chain. All of these signals are derived from the main accelerator clock (53 Mhz) by a combination of a DLL, multi-tap analog delay and programmable logic on the AFE board itself.

The digital signals from the discriminators serve as the inputs to the Central Track Trigger (CTT) and a bit is sent to the trigger system for every axial fiber every 132 ns (the time originally anticipated between beam crossings). This means that each AFE board is transmitting data at about 4.1 Gbits/s. The formatting and pipelining of this data is accomplished by sixteen CPLDs (complex programmable logic devices) in conjunction with four fast FIFO (first-in, first-out) memories. The trigger data is send over four LVDS (low-voltage differential signaling) links. Each LVDS link is driven by SN65LVDS95 transmitter chips. Each chip has 21 bits of parallel-load, serial-out shift registers driven by a 7x clock synthesizer and drives four LVDS lines (three line pairs are used to transmit 21 bits, the fourth carries the clock). With the data loaded into the transmitter chips with the 53 Mhz clock, the AFE can send  $21 \times 7 \times 4 = 588$  bits every 132 ns. One bit on each link is used to carry the 53 Mhz clock to help synchronize the data frames at the receiver end. This leaves  $20 \times 7 \times 4 = 560$  bits for trigger information. The actual discriminator information is carried by 512 bits. The other bits are used to send control information to the CTT. These include indication of which crossings had beam present, when a Level 1 accept was received from the trigger system, when the AFE is in a test mode or in reset, and so on. The control bits are duplicated on each of the four links and this redundancy is used to provide diagnostic information about the integrity of the links from the AFE to the CTT.

In total there are twenty CPLDs on each AFE. Besides the sixteen used to handle the discriminator data, one CPLD is used as a “virtual” SVXIIe chip to allow stored discriminator data to be read out on the same bus as the SVXIIe chips. Another CPLD is used to generate all the signals required to operate the SIFT chips and other timing signals for the board. The last two

CPLDs work in conjunction with a microcontroller on the AFE to implement communications with the monitoring and slow control system via the 1553 bus. The microcontroller is a mixed signal controller PIC14000 from Microchip [18]. It has an integrated single-slope 16-bit ADC which is used to monitor analog values on the board such as VLPC bias, VLPC current and VLPC temperature. The temperature of the VLPCs is measured via a calibrated carbon resistor mounted near the VLPC chips on every module. The value of the resistance must be measured to better than one part in a thousand and this drives the requirement for the ADC. The microcontroller implements closed-loop control for individual heater resistors on each VLPC module which allows the temperature at the VLPCs to be kept constant to  $9.00 \pm 0.05$  K despite larger cryostat temperature fluctuations. The VLPC temperature monitoring and control is performed by the right handed AFE boards. The VLPC bias voltage (which varies between 6 and 8 volts from module to module) must be controlled to  $\approx 50$  mV to achieve optimal detector performance.

The extensive use of programmable logic on the AFE (twenty CPLDs and a microcontroller) greatly eased the task of designing, building, and operating this very complicated board. It enabled the design of the AFE to be completed before all details of the interconnected detector systems were finalized. It allowed the fabrication of a single printed circuit board that is flexible enough to instrument three very different detectors. And it allows this very complicated board to operate with very little external control — once set points and operating parameters are downloaded, firmware on the board controls the system using on board DACs and ADCs. It also allows us to modify the firmware to optimize the operation of the electronics as running conditions change.

The performance of the electronics is dictated by the physics requirements of the detector. Due to the small diameter scintillating fibers used in the CFT coupled with the long waveguides necessary to direct the signals to the platform, the signals generated by the VLPCs can be small ( $\approx 10$  photoelectrons incident upon the VLPCs). To assure acceptable efficiency for triggers and tracking, the individual channel thresholds must therefore be set between 1.5 and 2 photoelectrons (pe). To maintain a low and stable threshold and to be able to distinguish individual photopeaks during calibration, the analog signal must be digitized with a noise of less than 0.4 pe or about 2 fC. In fact, the front end electronics are able to achieve or exceed all requirements. The mean pedestal width from fits to LED calibration spectra (as described in Section 2.2.6) for all axial fibers is 0.24 pe or 1.6 fC and discriminator thresholds have similar noise and offsets of less than 2 fC so that it is possible to set discriminator thresholds below 10 fC for most channels. A sample spectrum from calibration data is shown in Figure 11. A summary of the important parameters for the AFE is given in Table 2.

The readout of the SVXIIe chips mounted on the AFE boards is coordinated

Table 2  
Summary of AFE board characteristics

AFE overview	
Number of readout channels per AFE	512
Number of MCMs per AFE	8
Total number of parts on AFE	2300
Threshold settings (analog V generated by onboard DACs)	4 per MCM
Pedestal settings (analog V generated by onboard DACs)	1 per MCM
Output bandwidth (trigger)	4200 Mbit/s
Output bandwidth (SVXIIe bus)	159 Mbit/s
AFE performance	
Noise (input referred) — analog readout	1.6 fC
Noise (input referred) — discriminator	1.2 fC
Threshold spread (rms)	2 fC
Pedestal spread (rms)	3 fC
AFE stability and reliability	
Mean time between failures (estimated)	35000 hrs/board
Calibration stability	Better than 1%

via signals from the Sequencers and Sequencer Controllers. The sparsified data is transferred from the Sequencers to VME Transition Modules (VTM) in the movable counting house (MCH) via fiber optics cables. The VTMs transfer the data to buffers in VME Readout Buffers in VME crates. A VME Readout Buffer Controller mounted in the same crate controls the assignment of buffers. A Single Board Computer mounted in that crate serves as the interface to the higher level readout. The readout of the CFT and preshower detectors is buffered in a total of four VME crates in the MCH. Details of the higher level readout system are provided in Sections 2.1.1 and 10.4.

### 2.2.6 Calibration

The calibration system for the CFT [19] allows us to measure the gain of each fiber/VLPC channel, monitor the stability of the VLPCs over time, measure and track the attenuation length of each fiber, and was a useful debugging tool during commissioning of the detector.

Light from fast green LEDs [20] is introduced into the active core of the fibers through the cladding using flat optical panels, see Figure 12. ??? Need updated information on what happens The optical flat panels consist of a single thin ribbon of 0.01" diameter clear fibers which have been degraded along one side of the ribbon so that light is emitted through the cladding walls. At one end of the ribbon, the fibers are bundled together, potted and finished. The LED is located within a metal ferrule crimped to the end of the fiber bundle. The panels are 1" wide  $\times$  17.7" long and extremely light and flexible, conforming easily to the cylindrical surface of the CFT. The panels are assembled into bands, shown in Figure 13, which are mounted around all eight fiber cylinders, as shown in Figure 14. Each fiber ribbon is lit by three panels, allowing for redundancy and a large dynamic range.

### 2.2.7 Performance

The CFT is performing reliably, and more than 98% of the channels are operational. The probability of finding a hit on a track is better than 98%.

photoelectron yield and resolution

??? Cosmic ray testing is described in the TDR, but I expect further tests will be done once the CFT is completed. When that information is available, it will be included here.

The small fiber diameter gives the CFT an inherent doublet layer resolution of about 100  $\mu\text{m}$  as long as the location of the individual fibers is known to better than 50 $\mu\text{m}$ .

### 2.2.8 Level 1 Central Track Trigger

The Level 1 Central Track Trigger (CTT) uses data from the axial scintillating fibers, as well as the central and forward preshower detectors and provides information to the muon and calorimeter trigger systems [21,22]. The trigger is pipelined so that it is deadtimeless. The signals from the discriminators for all axial fibers are transmitted (as described in Section 2.2.5) to field programmable gate arrays (FPGAs). Hit coincidences between signals from all eight axial layers are identified as tracks if they are consistent with the passage of a particle with  $p_T > 1.5 \text{ GeV}/c$ . Tracks are combined with clusters from the central preshower detector to form an electron trigger and with hits in the muon detectors to form a muon trigger. To accomplish this level of tracking within the 4  $\mu\text{s}$  allowed for Level 1 processing, the CFT is divided into 80 equal azimuthal trigger sectors (TS) for parallel processing. ??? this section needs to be fleshed out too ???



Fig. 5. Routing of the clear waveguide fibers on the face of the central cryostat.

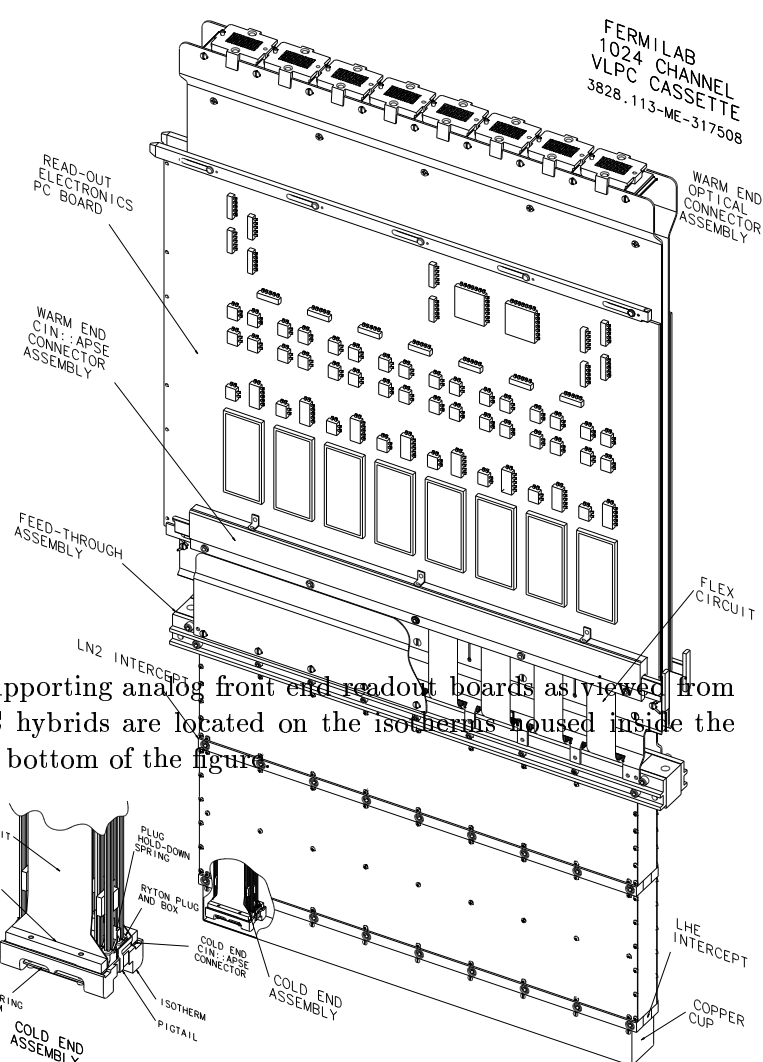


Fig. 6. VLPC cassette supporting analog front end readout boards as viewed from the left side. The VLPC hybrids are located on the isotherms housed inside the copper cup shown at the bottom of the figure.

Fig. 7. VLPC cassette body with left side body panel and side panels removed to show four installed modules.

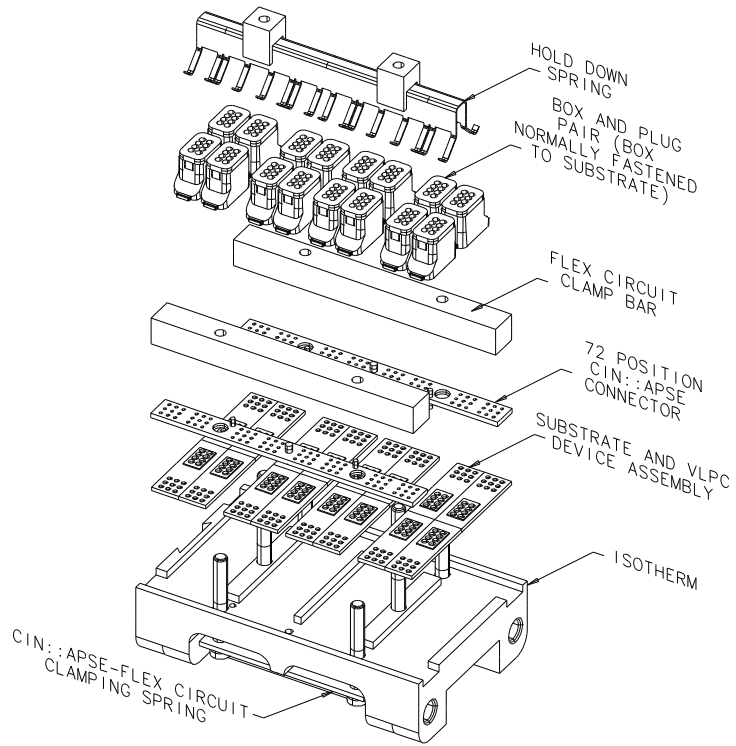


Fig. 8. Cold-end assembly for one 128-channel module of a VLPC cassette.

Fig. 9. Simplified schematic diagram of the SIFT chip. The bold text indicates clock signals supplied to the SIFT. VCLAMP, VTHR, and VREF are externally-supplied DC voltage levels.

Fig. 10. Photograph of an MCM showing the SVXIIe chip and two of the four SIFT chips.

Fig. 11. A typical LED spectrum for a single VLPC for an axial CFT fiber. Every channel is fit automatically and the parameters of the fit are extracted and used for offline reconstruction. Typically, more than 97% of the axial channels are fit successfully. The solid histogram is the data; the smooth curve is the fit.

Fig. 12. Calibration system for the CFT. Blue light emitted by the LED is dispersed via the flat optical panel. The dark circles represent fibers which absorb one or more blue photons; the open circles represent fibers which are not excited by the LED light.

Fig. 13. Assembly of flat optical panels into bands.

Fig. 14. Mounting scheme for the flat optical panels for the CFT calibration.

Fig. 15. Perspective view of the solenoid inside the central calorimeter. One end calorimeter and the corresponding end muon chambers have been omitted for clarity. Also shown are the service chimney and control dewar.

### 3 Solenoidal magnet

The superconducting solenoidal magnet was designed [23] to optimize the momentum resolution,  $\delta p_T/p_T$ , and tracking pattern recognition within the constraints imposed by the existing detector. The overall physical size of the magnet was determined by the available space within the central calorimeter vacuum vessel: 2.73 m in length and 1.42 m in diameter. We selected a central field of 2 T after considering the momentum resolution and tracking pattern recognition, the available space, and the thickness of the cryostat which depends on the thicknesses of the conductor and support cylinder. In addition, the magnet is required i) to operate safely and stably at either polarity, ii) to have a uniform field over as large a percentage of the volume as practical, iii) to be as thin as possible to make the tracking volume as large as possible, iv) to contain as little material as practical so as to preserve the electromagnetic energy resolution of the existing calorimeter, and v) to quench safely without a protection resistor (although one is installed). Services such as cryogenics, magnet high current buses, and vacuum pumpout and relief must reach the magnet from the control dewar through the narrow space (7.6 cm) between the central and end calorimeter vacuum vessels. The magnet system is controlled remotely, including cool down, energization, de-energization for field reversal, quench recovery and warmup, without access to the magnet cryostat, service chimney, or control dewar.

The major parameters of the solenoid design are listed in Table 3. A perspective view of the solenoid inside the central calorimeter with its chimney and control dewar is shown in Figure 15.

The solenoid, along with its cryostat, control dewar, and connecting service chimney, was manufactured by Toshiba Corp. in Yokohama, Japan.

#### 3.1 Magnet construction

The solenoid is wound with two layers of superconductor to achieve the required linear current density for a 2 T central field. The support cylinder is located on the outside of the windings to support the radial Lorentz forces on the conductor and provide axial rigidity to the finished coil. To maximize the field uniformity inside the bore of the magnet, the current density in the windings is larger at the ends of the coil. This is accomplished by the use of two conductors whose only difference is in the width of the aluminum stabi-

Table 3  
Major parameters of the solenoid

Central field	2.0 T
Operating current	4820 A
Cryostat warm bore	1.067 m
Cryostat length	2.729 m
Integrated field homogeneity	$\pm 5.0 \times 10^{-3}$
Stored energy	5.6 MJ
Inductance	0.48 H
Cooling	Indirect, 2-phase forced flow helium
Cold mass	$\approx 1500$ kg
Conductor	18 strand Cu:NbTi, cabled
Conductor stabilizer	High purity aluminum
Transparency	$0.9 X_0$
Cooldown time	$\leq 120$ hours
Magnet charging time	$\leq 30$ minutes
Fast discharge time constant	$\leq 15$ seconds
Slow discharge time constant	$\leq 330$ seconds
Total operating heat load	$\leq 18$ W plus 1 g/s liquefaction
Operating helium mass flow	$\leq 4$ g/s

Fig. 16. Cross sections of the two conductors used in construction of the solenoidal magnet.

lizer. Cross sectional views of the conductors are shown in Figure 16. Both conductors are made with a superconducting Rutherford [24] cable of multifilamentary Cu:NbTi strands stabilized with pure aluminum. The basic strand has a Cu:NbTi ratio of 1.3:1 and a diameter of 0.808 mm; sixteen strands are used in each conductor. The larger conductor is 5.125 mm wide and the smaller is 3.920 mm wide; both have a radial height of 15 mm for ease of forming joints and winding. The superconductor is placed near the inside radius of the conductor to maximize the region of aluminum that can be used for making welded joints between conductor lengths during coil winding.

Both conductors are used in both layers. The middle section of each layer is wound with the wider conductor and the end sections with the narrower conductor. The transition point between the two conductors in the inner layer occurs at  $z = \pm 0.953$  m, and at  $z = \pm 0.653$  m in the outer layer. Therefore,

there are four places in the solenoid where the conductor width changes. At these locations, the two grades of conductor are joined with a lap joint and edge-welded. The welding of a 40 cm length is done along the one overlapping turn of both grades of conductor in the four locations. Each joint entails the effective loss of one turn. There are no other joints in the coil.

### *3.2 Magnet cryostat*

The magnet cryostat consists of four major components: the vacuum vessel, the liquid-nitrogen-cooled radiation shield, the cold mass support system with liquid-nitrogen-cooled intercepts, and the helium cooling tube on the outer support cylinder of the superconducting coil.

The vacuum vessel consists of inner and outer coaxial aluminum shells with flat annular bulkheads welded to each end. The superconducting buses from the coil and the cryogen pipes from the outer support cylinder and the radiation shields leave the vacuum vessel through the service chimney nozzle welded in the bulkhead at the south end of the cryostat. The cryostat is designed for full internal vacuum and for an internal relieving pressure of 0.44 MPa (6.4 psig).

The magnet cold mass, the superconducting coil and outer support cylinder, weighs 1.46 metric tons. The cold mass support system consists of axial members which locate the coil axially and support it against axial thermal, decentering, and seismic forces, and nearly tangential members that locate the coil radially and provide radial support against thermal, gravitational, seismic, and decentering forces. The support members connect the outer support cylinder of the coil to the flat annular bulkheads of the vacuum vessel. All cold mass supports have thermal intercepts that operate near 87 K and the radial supports have a thermal intercept below 10 K. The magnet cryostat is attached to the central calorimeter by support brackets which carry the weight of the cryostat and the tracking detectors which are attached to it.

### *3.3 Control dewar and refrigeration system*

The control dewar is the interface between the permanently installed building piping and the movable detector. It has bayonet connections for cryogenic lines and contains the vapor-cooled current leads and a liquid-helium reservoir, supply-line subcooler, supply Joule-Thompson valve, and other valving and instrumentation. The current leads must carry the full design operating current of the magnet and are designed for safe operation without cooling gas flow for at least the full slow-discharge time constant of the magnet (approximately 300 s) in the event that cooling flow is lost while the magnet is

energized.

Cryogenic and electrical services are carried from the control dewar to the magnet cryostat via the service chimney, which also serves as the relief line for the solenoid vacuum space and provides a path for pumpout of the magnet cryostat and control dewar vacuum spaces. A cryogenic refrigeration system supplies liquid nitrogen and liquid helium to the magnet and liquid helium to the VLPCs used to read out the CFT (see Section 2.2). The two systems were considered together when the refrigeration system was designed.

The cryogenic system for the original DØ detector supplied liquid-nitrogen refrigeration to the three calorimeter cryostats and provided for the storage of the liquid argon used by the calorimeters. The original liquid-nitrogen storage dewar has adequate capacity (75.7 kL) for the needs of the calorimeters, the magnet cryostat, the VLPC cryostats, and a helium refrigerator/liquefier.

A standard Fermilab satellite stand alone refrigerator (STAR) provides helium refrigeration. The capacity of the STAR is sufficient for non-simultaneous cooldown and simultaneous operation of both the solenoid and VLPC systems. Liquid helium is stored in a 2000 L dewar which supplies the magnet control dewar and the VLPC cryostats via separate transfer lines.

### *3.4 Magnet energization and control*

A block diagram of the DC energization system is shown in Figure 17. The Power Energy Industries 150 power supply is a special Fermilab unit designed for superconducting loads. It is a twelve-phase-thyristor water-cooled rectifier unit with precision feedback current regulation. The power supply taps are set at 15 V/5000 A for efficient operation and reduced AC loading and DC ripple. The power supply regulates the current to within 0.01% using an external precision Holec 5000 A transducer installed downstream of the ripple filter and dump resistor.

Magnet polarity is reversed using a 5000 A DC mechanical motorized polarity reversing switch and a switch controller. Polarity reversal requires a slow discharge and recharging of the solenoid. The switch measures approximately 4 feet on a side, is floor-mounted, and requires no water cooling. The controller confirms that the polarity reversal occurs at zero current load and that the power supply is turned off. Polarity reversal takes about forty minutes and once the procedure is started, it must be completed before the original polarity can be restored.

The original DØ Texas Instruments TI565T Programmable Logic Controller (PLC) has been expanded to control and monitor the VLPC, solenoid, and

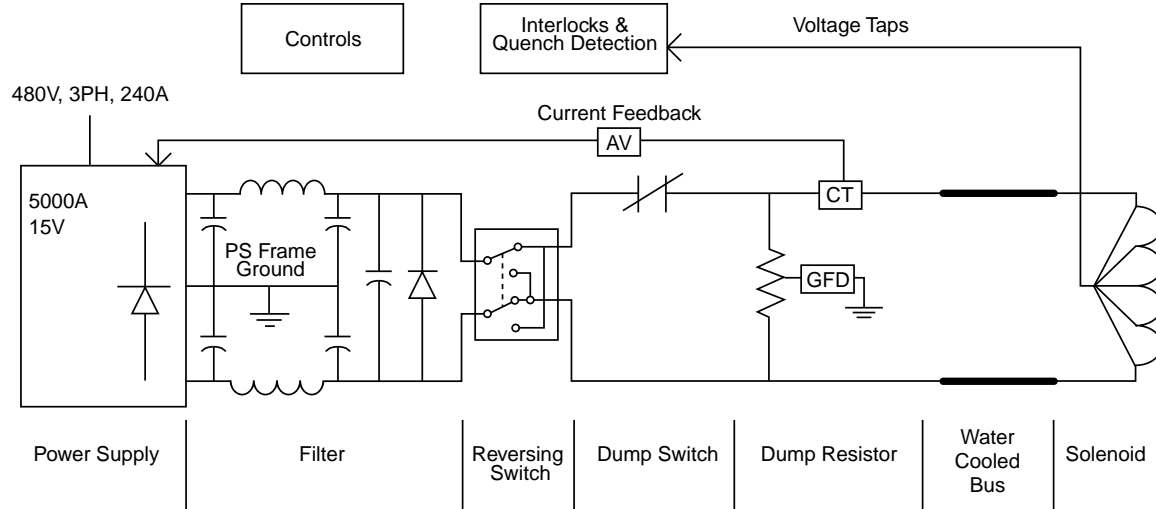


Fig. 17. Block diagram of the DC energization system for the solenoid.

helium refrigeration systems as well as the liquid argon cryogenics system and the cryogenics subsystems (e.g. vacuum, compressed air, and the oxygen deficiency hazard warning system). The PLC is a stand-alone system with an internal battery-backed program memory which requires no host system to download the control programs in the event of a power failure. It consists of two independent TI565T processors operated in a “hot backup” configuration. One PLC is online and actively controlling the system; the second is in standby, running step-for-step with the online unit but with its input/output communication disabled. Each PLC runs continuous internal diagnostics for errors. When a fatal error is registered by the active PLC, it is taken offline and the standby PLC is put online without intervention or disruption to the system.

Control of the helium refrigeration system and the magnet cryogenics was added to the TI565T PLC; dedicated control and monitoring of the magnet energization and protection system is done by a new Texas Instruments TI555 PLC. A quench protection monitor (QPM) hardwired chassis and interlock logic unit provide primary quench protection for the magnet. The QPM contains filtering, signal averaging, and delay circuitry for the potential taps and thermometry which are used in the quench detection logic, vapor-cooled lead fault detection, or power supply failure logic. It contains preset limits for selected sensors which trigger fast discharge of the magnet and it preserves the time ordering of the detected fault signals which trigger magnet discharge. The QPM defines a set of interlock conditions that must be satisfied before the magnet can be energized or the reversing switch operated.

DØ cryogenic controls are powered by a 10 kVA uninterruptable power supply which is backed up by an automatic diesel power generator. The total power consumption is approximately 6 kVA.



### 3.5 *Magnetic field*

The magnetic field of the full magnet system is modeled using the TOSCA [25] program. The calculated field map was compared with the measured field in two locations: near the internal radius of the solenoid cryostat ( $z \approx 58$  cm) at  $z = 0$ , and in the central gap at the top of the CF magnet yoke. Within the solenoid, the measured field was  $20.14 \pm 0.05$  kG; the calculated field at this location is 20.12 kG, the same within errors. There was a 4.6% difference between the calculated and measured field at the CF gap, requiring an adjustment in the calculated field for the CF toroid. A  $y - z$  view of the magnetic field is shown in Fig. 18. In the figure, the field lines begin at  $x = 0$  in the center of the solenoid, the left and right line ends differ by up to 2.5 m in  $x$ .

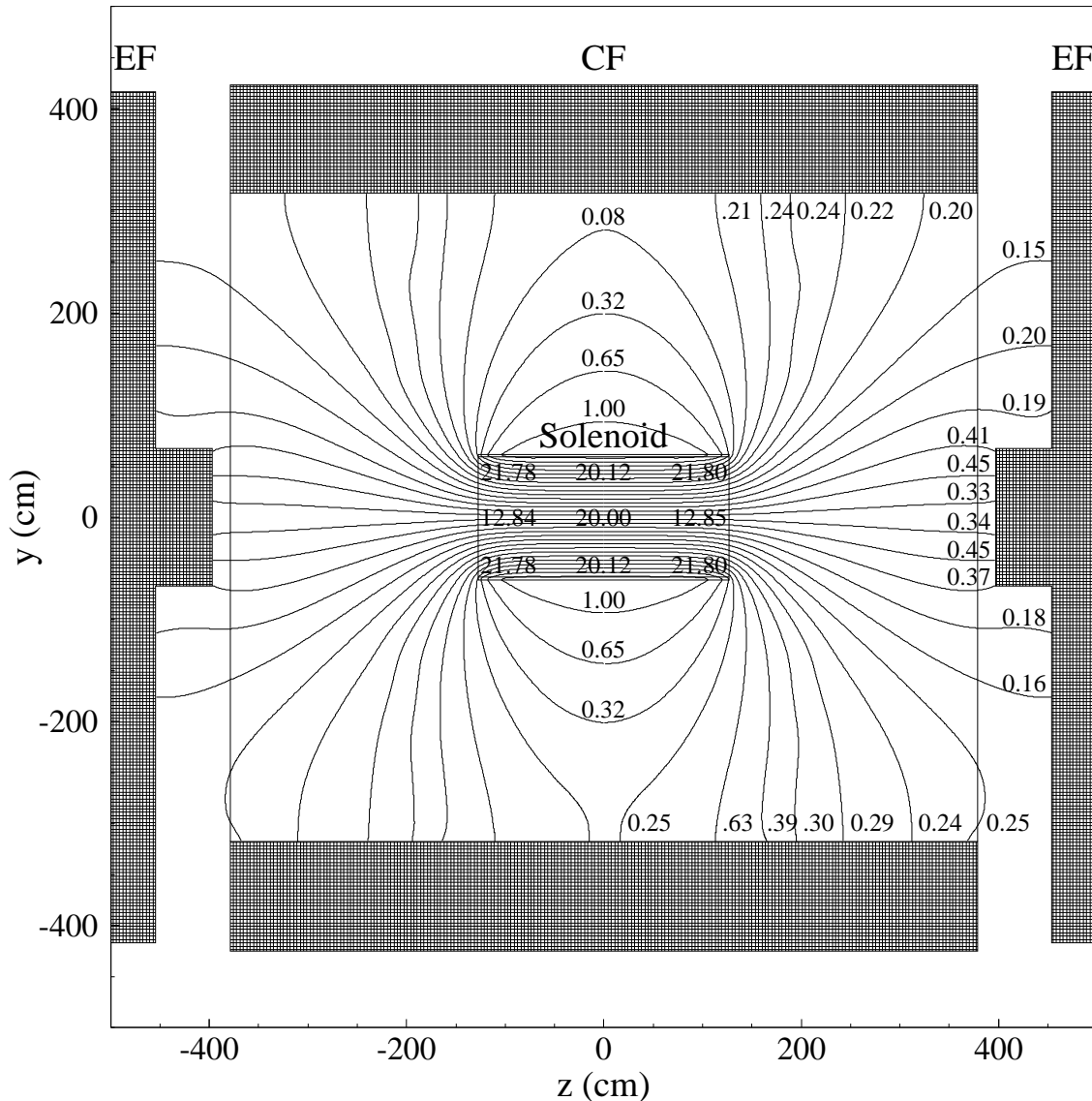


Fig. 18.  $y - z$  view of the DØ magnetic field. The field lines are projections onto the  $y - z$  plane; the left and right line ends differ by up to 2.5 m in  $x$ .

## 4 Preshower detectors

The preshower detectors aid in electron identification and background rejection during both online triggering and offline reconstruction. They function as both calorimeters and tracking detectors, providing better spatial matching between CFT or SMT tracks and preshower detector track stubs and showers than the calorimeters allow. The central preshower detector (CPS) covers the region  $|\eta| < 1.3$  and is located between the solenoid and the central calorimeter while the two forward preshower detectors (FPS) [26] cover  $1.5 < |\eta| < 2.5$  and are attached to the faces of the forward calorimeters. Their fast energy and position measurements allow us to include preshower infor-

Fig. 19. Cross sections of the CPS and FPS scintillator strips. The circles show the location of the embedded wavelength-shifting fibers.

mation in the Level 1 trigger, as well as correct the EM energy measurement of the central calorimeter for energy loss in the solenoid.

#### 4.1 *Common properties of the preshower detectors*

Both preshower detectors are made from interlocking triangular strips of scintillator, as shown in Figure 19. Since the triangles are interleaved, there is no dead space between strips and most tracks traverse more than one strip, allowing for excellent position measurement. The strips are made by extruding polystyrene plastic doped with 1% p-terphenyl and 150 ppm diphenyl stilbene, similar to Bicron BC-404 scintillator. Each scintillator strip is wrapped in aluminized mylar for optical isolation and the end of each strip is painted white. The packing density is different for the CPS and the FPS modules, resulting in different layer thicknesses and strip pitches. The pitch is 3.54 mm for the axial CPS module and 3.65 mm for the FPS. After extrusion and wrapping, the triangular strips have a tendency to bow. To relieve stress in the plastic, making them easier to handle, the strips are slumped to the required shapes by heating to 180° F for two hours followed by slow cooling.

Embedded at the center of each scintillator strip is a wavelength-shifting fiber which collects and carries the light to the edge of the module where it is connected to a clear light-guide fiber which transfers the light to a VLPC for readout. The WLS fibers are 835  $\mu\text{m}$  diameter Kuraray multiclاد fibers and the light-guide fibers are Kuraray multiclاد S-type fibers with the same diameter.

##### 4.1.1 *Readout electronics*

The preshower detectors are read out using VLPCs and SVXIIe chips, as described above for the CFT and SMT detectors. The CFT needs sensitivity only to minimum ionizing particles, but the preshower detectors detect both minimum ionizing particles and measure electromagnetic showers over a wide energy range. The energy deposition from a 10 GeV electron can be as low as a few MIPs, while a 100 GeV electron may deposit several hundred MIPs in a single strip. In practice, however, saturation above 50 MIPs has little effect on the position and energy resolution of the shower. Assuming a factor of two difference in the response due to angle effects (???), a dynamic range of 1–100 MIPs is required.

??? TDR p. 56 describes a specific preshower chip - was this built???

Fig. 20. The CPS unwrapped in a plane. Each rectangle (trapezoid) is one octant module of the axial (stereo) layer. Note that the stereo octant edges are precisely aligned with the axial octant edges.

Fig. 21. Schematic drawing of the CPS light block.

## 4.2 Central preshower detector

The CPS consists of three concentric cylindrical layers of triangular scintillator strips and is located in the 510 mm gap between the solenoid and the central calorimeter. Between the solenoid and the CPS is a Pb radiator approximately  $1X_0$ -thick. The solenoid itself is  $1X_0$  thick, providing a total of about two radiation lengths of material for particles at normal incidence.

The three layers of scintillator are arranged in an axial- $u-v$  geometry, with a stereo angle of about  $\pm 23^\circ$ . Each layer contains 1280 strips. The WLS fibers are split at  $z = 0$  and read out from each end resulting in 2560 readout channels/layer. The non-readout ends of the fibers are diamond-polished and silvered. At the readout end, fibers are grouped into bunches of sixteen and potted into connectors for transition to the clear light-guide fibers. The channel count and geometry of the CPS matches that of the CFT for Level 1 triggering purposes. Each group of sixteen WLS fibers from the CPS axial layer corresponds to one of the eighty CFT sectors in  $\phi$ . As with the CFT, the stereo layers are not used at Level 1.

Each layer is made from eight octant modules. The modules consist of two  $1/32$ " stainless steel skins with the scintillator strips sandwiched in between. The ends of the stereo modules align to the ends of alternating axial modules, as shown in Figure 20. The modules are attached directly to the solenoid by bolts at each corner. Eight  $\frac{1}{4}$ " pins at each end of the solenoid provide additional registration. Connector blocks are spot welded between the stainless steel skins. The blocks provide structural integrity to the end region of the modules and mounting locations for the WLS connector and the cover for the light-guide connector.

### 4.2.1 Calibration

Each bundle of WLS fibers runs over a light block as shown in Figure 21.

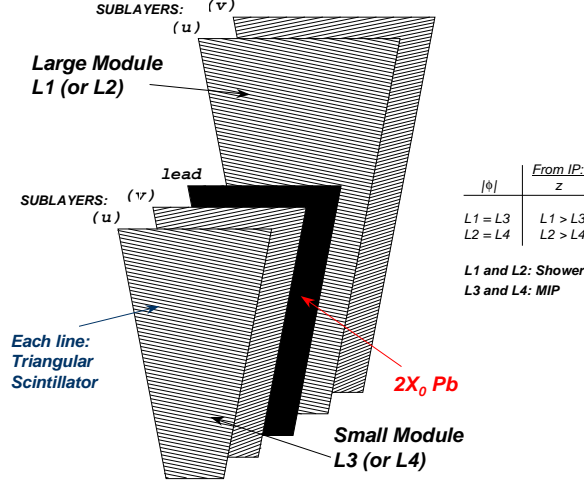


Fig. 22. FPS module layer showing the  $u - v$  MIP and shower layers, separated by an absorber.

#### 4.3 Forward preshower detector

The two FPS detectors are mounted on the spherical heads of the EC cryostats, between the  $L\emptyset$  luminosity counters at the inner edge and the intercryostat detectors (ICD) at the outer edge. Each detector is made from two layers of a double layer of scintillator strips, separated by a  $2X_0$ -thick lead-stainless-steel absorber, as shown in Figure 22. The upstream layers are known as the minimum ionizing particle, or MIP, layers and the downstream layers, those behind the absorber, are called the shower layers. All charged particles passing through the detector will register a minimum ionizing track in the MIP layer, allowing measurement of the location (in  $\eta$ ,  $\phi$ , and  $z$ ) of the track. Electrons will readily shower in the absorber, leading to a cluster of energy in the shower layer that is spatially matched with the MIP-layer signal. Heavier charged particles are less likely to shower, producing a second MIP signal in the shower layer. Photons will not interact in the MIP layer, but will produce a shower signal in the shower layer. The MIP layers, and the absorber, cover the region  $1.65 < |\eta| < 2.5$ . The outer region of the FPS,  $1.5 < |\eta| < 1.65$ , lies in the shadow of the solenoidal magnet coil, which provides up to  $3X_0$  of material in front of the FPS. This amount of material readily induces showers which can be identified in the shower layers of the detector. Figure 23 shows typical GEANT-simulated signatures for 50 GeV electrons and pions traversing the FPS.

Each of the thirty-two modules for each FPS detector is independently housed in a wedge-shaped aluminum support frame, as shown in Figure 24. Eight modules form a single, structurally distinct, FPS layer that conforms to the face of the end calorimeter cryostat. Each layer consists of alternating  $22.5^\circ$  wedges of active and inactive material. Successive layers are offset, with an

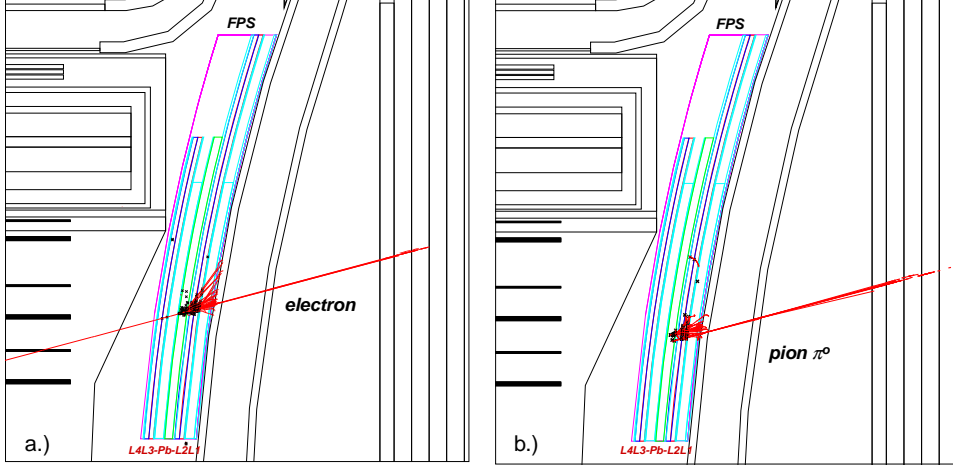


Fig. 23. Typical GEANT-simulated signatures of 50 GeV a) electrons and b) neutral pions traversing the FPS detector.

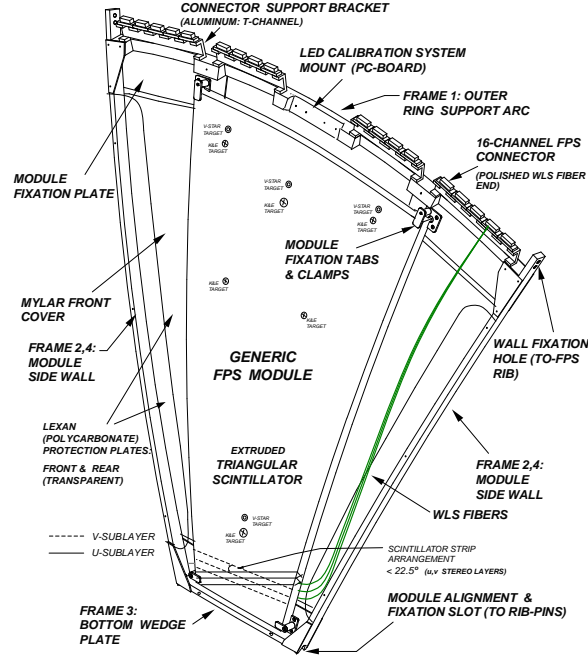


Fig. 24. Three-dimensional view of the supporting frame of an FPS module.

0.5" overlap between the active areas of the modules, and module boundaries are oriented to match the  $\phi$  geometry of the EM calorimeter modules. Each module consists of two sublayers of nested scintillator strips with a crossing ("stereo") angle of  $22.5^\circ$  with respect to one another. The strips in the two stereo layers are perpendicular to one of the edges of a module and form an angle of  $78.75^\circ$  with the vertical bisector of a module. Figure 25 shows an  $r - \phi$  view of two layers of the north FPS detector.

As can be seen in Figure 25, each detector has a cut-out region to allow the passage of solenoid support services. Thus, FPS modules come in three sizes:

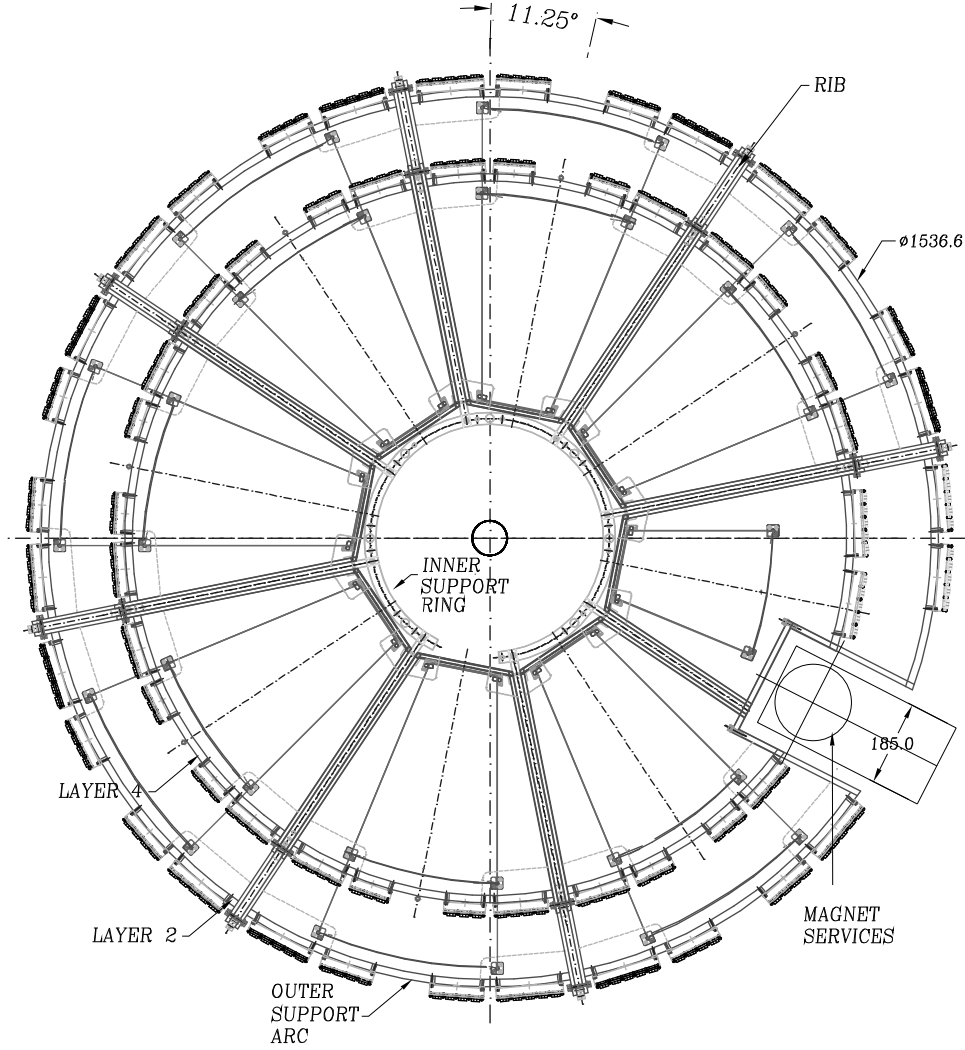


Fig. 25.  $r - \phi$  view of the north FPS detector. For clarity, only layers 2 and 4 are shown; layers 1 and 3 are rotated by  $22.5^\circ$  in  $\phi$  with respect to these layers. The south FPS detector is a mirror image of the north detector.

those in the MIP layers, those in the shower layers, and four smaller, “special,” modules for each detector which cover  $1.8 < |\eta| < 2.5$ . The two modules in successive  $\phi$  layers and the dimensions of the three types of modules are shown in Figure 26.

The lead absorber layer is divided into forty-eight wedge-shaped segments, each subtending  $7.5^\circ$  in  $\phi$ . Each segment consists of two lead absorber elements epoxied to each side of a  $1/8$ ”-thick stainless-steel plate. Each steel plate is approximately 0.5” longer radially than the lead plates, to allow connection to inner and outer support rings that are nested within the overall FPS layers. The total thickness of a lead-steel-lead segment is 11 mm, or  $2X_0$ . The  $\phi$  edges of each segment are beveled to allow nesting of adjacent segments with minimal non-projective gaps between them.

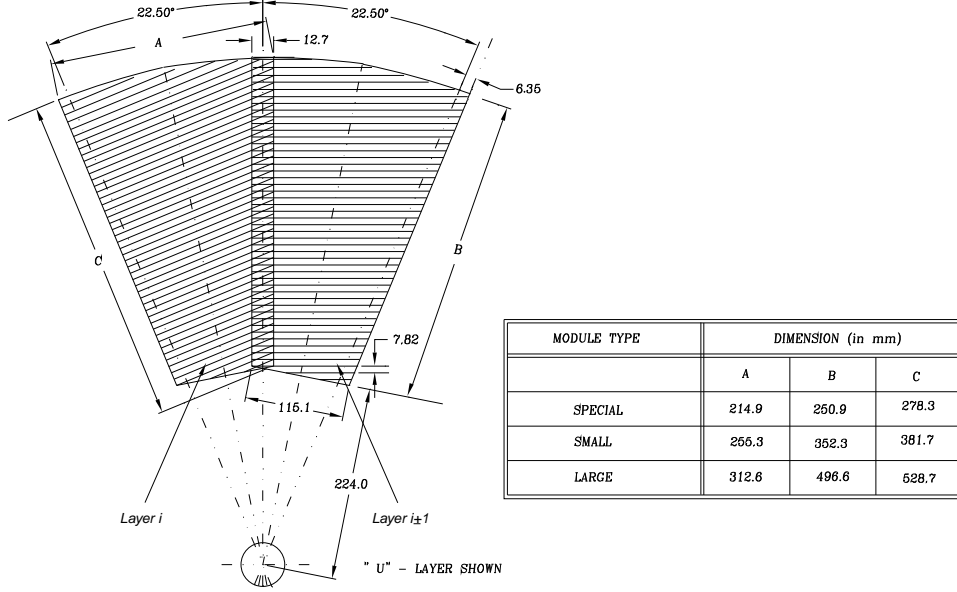


Fig. 26. Orientation of two modules in successive FPS layers. The 0.5" overlap region is shown, along with the dimensions of the three types of modules.

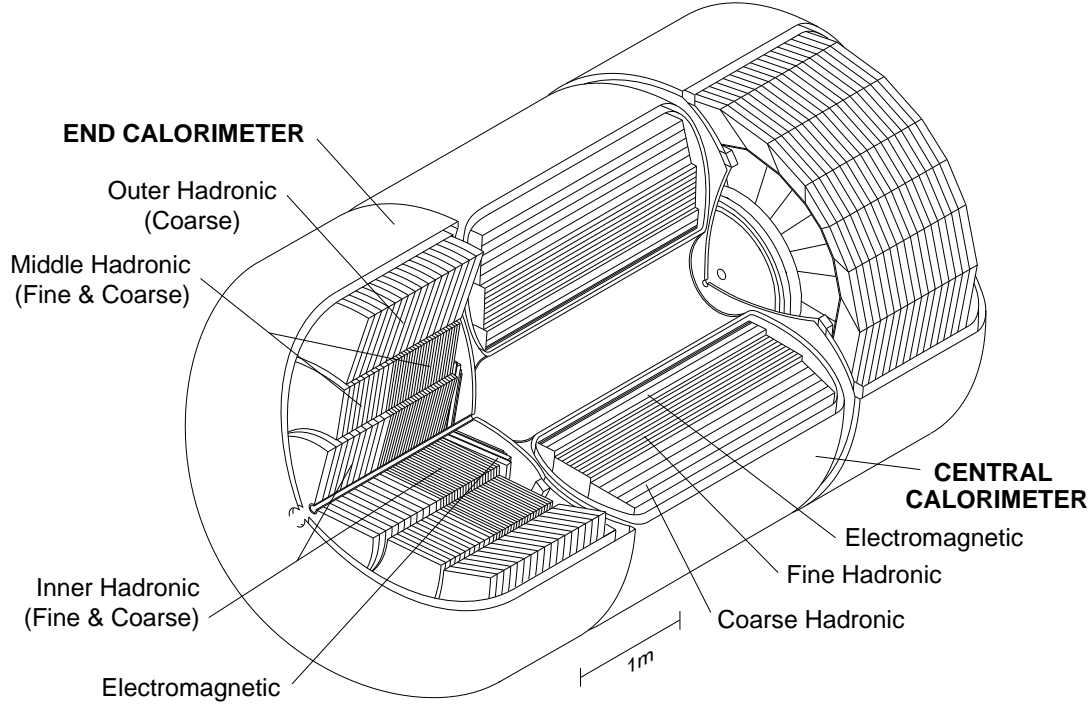
## 5 Calorimeters

The calorimeters were designed to provide the energy measurement for electrons, photons, and jets in the absence of a central magnetic field (as was the case during Run I of the Tevatron), as well as assist in the identification of electrons, photons, jets and muons and establish the transverse energy balance in an event. The calorimeters themselves are unchanged from Run II and are described in detail in Ref. [8].

As shown in Fig. 27, the central calorimeter (CC) covers roughly  $|\eta| \leq 1$  and two end calorimeters, ECN (north) and ECS (south), extend coverage to  $|\eta| \approx 4$ . Each calorimeter contains an electromagnetic section closest to the interaction region followed by fine and coarse hadronic sections whose resolution decreases with distance from the interaction region. The active medium for all of the calorimeters is liquid argon and each of the three calorimeters (CC, ECN, and ECS) is located within a cryostat that maintains the temperature at approximately 80 K. Different absorber plates are used in different locations. The electromagnetic sections (EM) use thin (3 or 4 mm) plates, made from nearly pure depleted uranium. The fine hadronic sections are made from 6-mm-thick uranium-niobium (2%) alloy. The coarse hadronic modules contain relatively thick (46.5 mm) plates of either copper (CC) or stainless steel (EC). Except at the smallest angles in the EC, 16 or 24 modules of each type are arranged in a ring.

A typical calorimeter cell is shown in Fig. 28. The electric field is established by grounding the metal absorber plates and connecting the resistive surfaces





Blessing fig.5 4/21/03KF.ai

Fig. 27. Isometric view of the central and two end calorimeters.

of the signal boards to positive high voltage (typically 2.0–2.5 kV). The electron drift time across the 2.3 mm gap is approximately 450 ns (??? are these numbers still correct?). Signal boards for all but the EM and small-angle hadronic modules in the EC are made from two 0.5 mm G-10 [27] sheets. One surface of each board is coated with carbon-loaded epoxy [28] with a typical sheet resistivity  $40 \text{ M}\Omega/\square$ . One of the inner surfaces is bare G-10; the other, originally copper-coated, is milled into the pattern necessary for segmented readout. Several such pads at approximately the same  $\eta$  and  $\phi$  are ganged together in depth to form a readout cell. The transverse size of the readout cells are comparable to the transverse sizes of showers: 1–2 cm for EM showers and about 10 cm for hadronic showers. The scale in  $\eta$  and  $\phi$  is set by the typical size of parton jets,  $\Delta R = \sqrt{\Delta\eta^2 + \Delta\phi^2} \approx 0.5$ . Segmentation finer than this is useful in probing the shape of jets. Longitudinal subdivisions are useful since longitudinal shower profiles help distinguish electrons and hadrons.

Calorimeter readout modules form pseudo-projective towers as shown in Fig. 29, with each tower subdivided in depth. We use the term “pseudo-projective” because the centers of cells of increasing shower depth lie on rays projecting from the center of the interaction region, but the cell boundaries are aligned perpendicular to the absorber plates. There are four separate depth layers for the

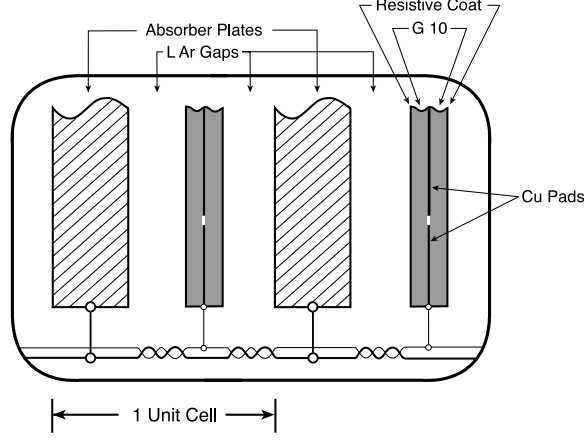


Fig. 28. Schematic view of the liquid argon gap and signal board unit cell for the calorimeter.

EM modules in the CC and EC. The first two layers are typically two radiation lengths ( $X_0$ ) thick and help measure the longitudinal shower development near the beginning of showers where photons and  $\pi^0$ s differ statistically. The third layer spans the region of maximum EM shower energy deposition and the fourth completes the EM coverage of approximately  $20X_0$ . The fine hadronic modules are typically segmented into three or four layers; coarse hadronic modules are ganged into one or three layers. Each layer of modules is offset from the others to prevent through-going azimuthal cracks. Typical transverse sizes of towers in both EM and hadronic modules are  $\Delta\eta = 0.1$  and  $\Delta\phi = 2\pi/64 \approx 0.1$ . The third section of the EM modules is segmented twice as finely in both  $\eta$  and  $\phi$  to allow more precise location of EM shower centroids. All modules are offset to prevent through-going azimuthal cracks.

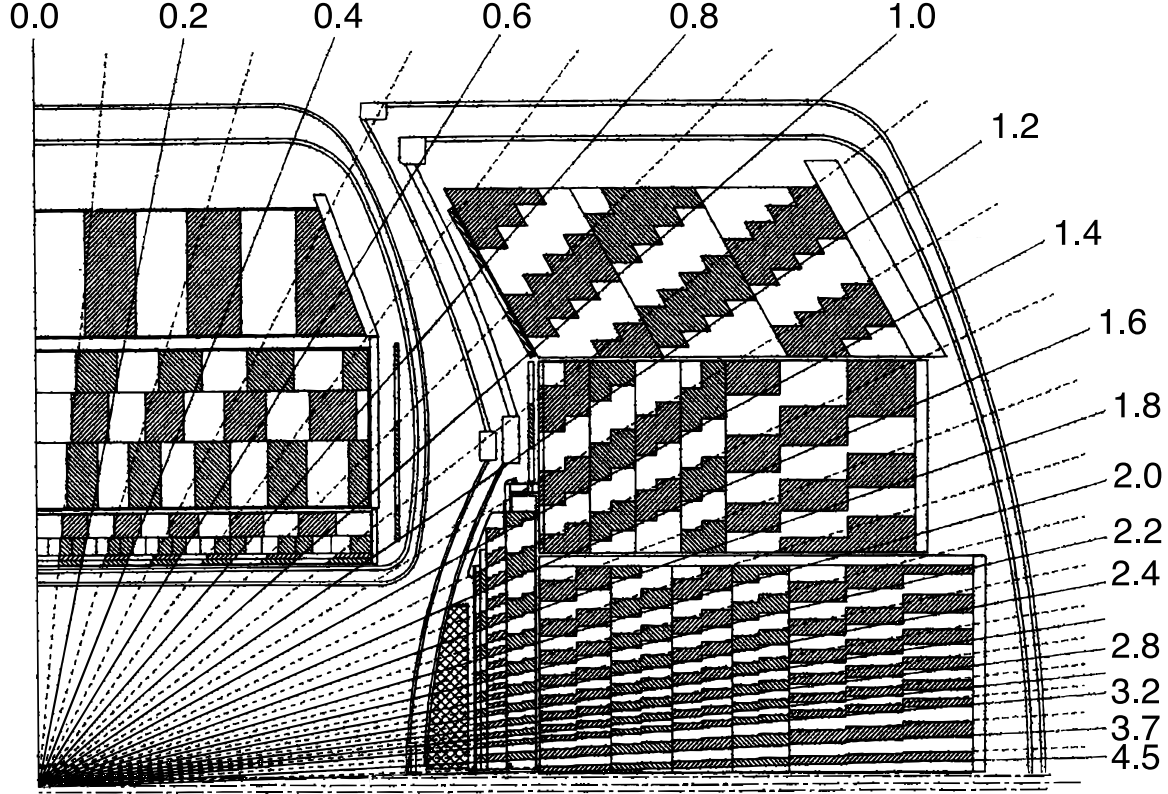


Fig. 29. Schematic view of a portion of the DØ calorimeters showing the transverse and longitudinal segmentation pattern. The shading pattern indicates cells for signal readout. The rays indicate the pseudorapidity intervals seen from the center of the detector.

## 6 Inter-Cryostat Detector

The DØ liquid argon calorimeter system is contained in three separate cryostats. The central cryostat (CC) provides complete electromagnetic and hadronic sampling in the pseudorapidity ( $\eta \equiv -\ln \tan(\theta/2)$ ) region  $-0.8 < \eta < 0.8$ . The end cryostats (EC) provide full sampling in the region  $1.4 < |\eta| < 4.0$ . The intermediate region  $0.8 < |\eta| < 1.4$  is covered partially by modules in the central cryostat and partially by overlapping modules in the end cryostats.

Because of the triple-cryostat design of the DØ calorimeter, there is substantial unsampled material in the intermediate region, which degrades energy resolution. In order to solve this problem, additional layers of sampling are located between the cryostats. One layer is inside the central cryostat and called the central massless gap (CCMG). Another layer is inside the end cryostat and referred to as end cryostat massless gaps (ECMG). A third layer of scintillator sampling used between the cryostats is called the Inter-Cryostat Detector (ICD). The ICD is attached to the exterior surface of the end cryostats, and covers the pseudorapidity region  $1.1 < |\eta| < 1.4$ . Figure 2 shows the central

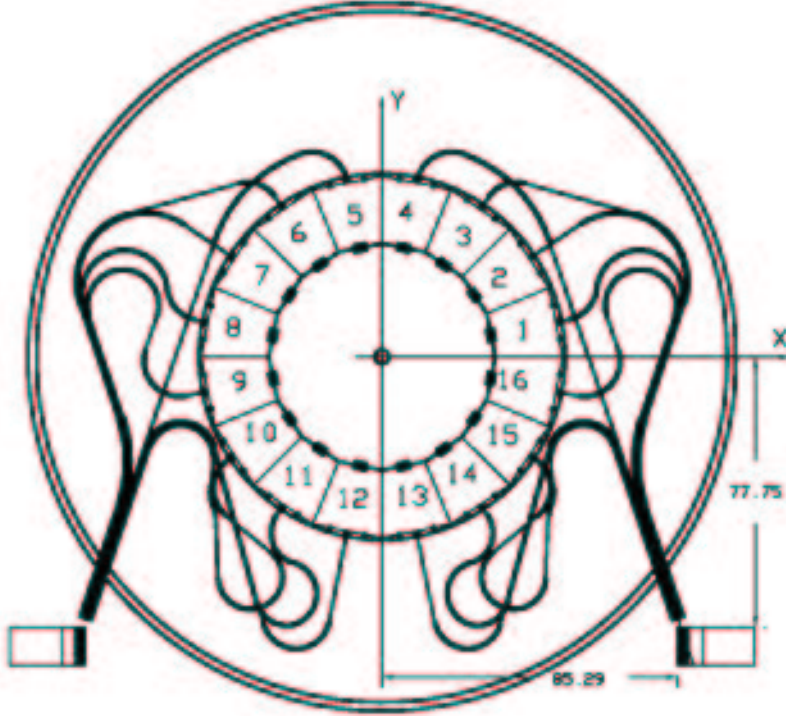


Fig. 30. The arrangement of the ICD tiles on the endcap cryostat.

region of the DØ detector, including the ICD.

The ICD is a series of scintillating tiles connected to readout electronics devices via wavelength-shifting and clear plastic fibers. The light from the passage of a charged particle through a scintillating tile is passed to the wavelength-shifting fibers. The wavelength-shifting fibers are mated to clear optical fibers at the outer radius on the ICD tile enclosure. The clear fibers terminate at a photomultiplier tube (PMT) connected to the back of the readout electronics. The PMT then sends this signal through the electronics motherboard to the pre-amplifier. The pre-amplifier shapes the signal and sends it out of the ICD to a central processing bank. A schematic of the ICD tile layout is shown in Fig. 30. In this figure, the beam line is perpendicular to the page. The ICD scintillator tiles are numbered counterclockwise.

Because of the solenoidal magnetic field (with no return yoke), the readout electronics for the ICD have to be located away from the tiles. The electronics are contained in a drawer system, located in a low-field region to the side of the calorimeter. An ICD drawer houses PMTs, PMT electronics, and preamplifiers for six channels of readout. The readout signals are then multiplexed to interface with the BLS system common to the rest of the calorimeter. An ICD crate houses a two-dimensional array of slots holding sixteen ICD drawers. Each drawer slides individually on rails, making individual maintenance of each drawer easy. Internally, the ICD drawers have fibers impinging on the PMTs from the back end through the fiber backplane.

Clear fibers from the ICD tiles are mated to clear fibers contained in a light-tight enclosure called the “fiber backplane.” Between the fiber backplane and the crate containing the drawers is a block of iron, with holes drilled to accept the PMTs. Fibers from the fiber backplane terminate in mounts (called cookies) in the iron. When a drawer is in the tray, six PMTs will be aligned with six fiber bundles (two per channel plus one for a calibration signal) from the backplane. The PMTs are spring-loaded to ensure good contact with the fibers. The iron block, in combination with tubular magnetic shields, protects the PMTs from any fringe magnetic fields in the region of the electronics drawers. O-rings at the base of the PMTs and the drawers themselves provide a dark environment for the PMTs.

The PMT high voltage dividers and preamplifiers are located on daughter cards that plug into the motherboard, which facilitates replacement. Input high voltage and output signal ports are located on the front of the drawer. Temperature monitors are placed between pairs of drawers to monitor heat dissipation from the pre-amplifiers. The readout path of a channel of the ICD is shown schematically in Fig. 31, while Fig. 32 shows the layout of the ICD drawers.

The signal electronics are designed to be compatible with the DØ upgrade BLS/ADC system and electronics calibration. The ICD uses a modified version of the upgrade calorimeter preamplifiers, designed to stretch the PMT signal into a signal similar to that of the liquid argon readout. A modified form of the electronic pulsar system is used to calibrate the preamplifier signals as well as to monitor performance of the electronics and verify that all channels are working. The response of the PMTs are monitored using an LED flasher system, similar in design to the LED flashers used for the muon trigger scintillators. An LED flasher is housed in each of the four fiber backplanes, and the level of the light signal is controlled externally.

The ICD layer of the calorimetry is designed to restore energy loss due to the poor coverage in the cryostat overlap region. ICD sampling weights are tuned to jet energy, using di-jet  $E_T$  balance. In Fig. 33, the effect of the ICD sampling is shown, as a function of the detector pseudorapidity.

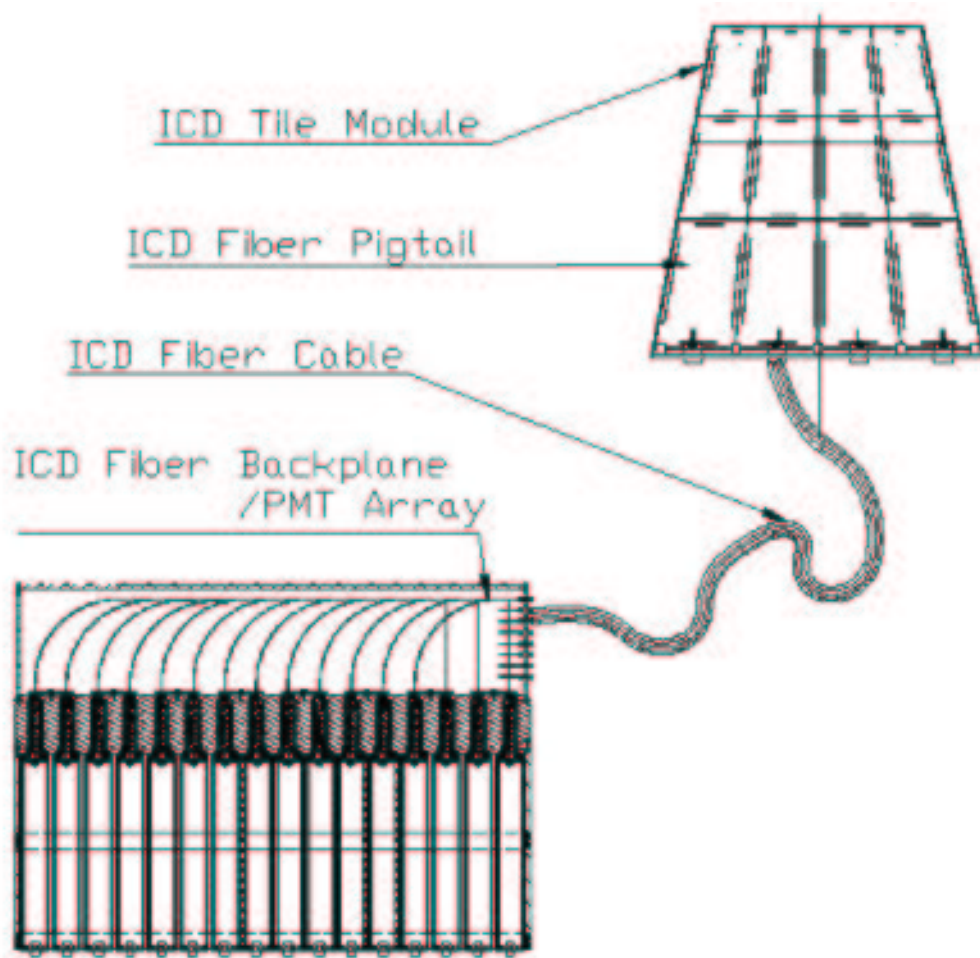


Fig. 31. The layout of an ICD readout channel, from tile through fibers to the PMT mounted on the electronics drawers

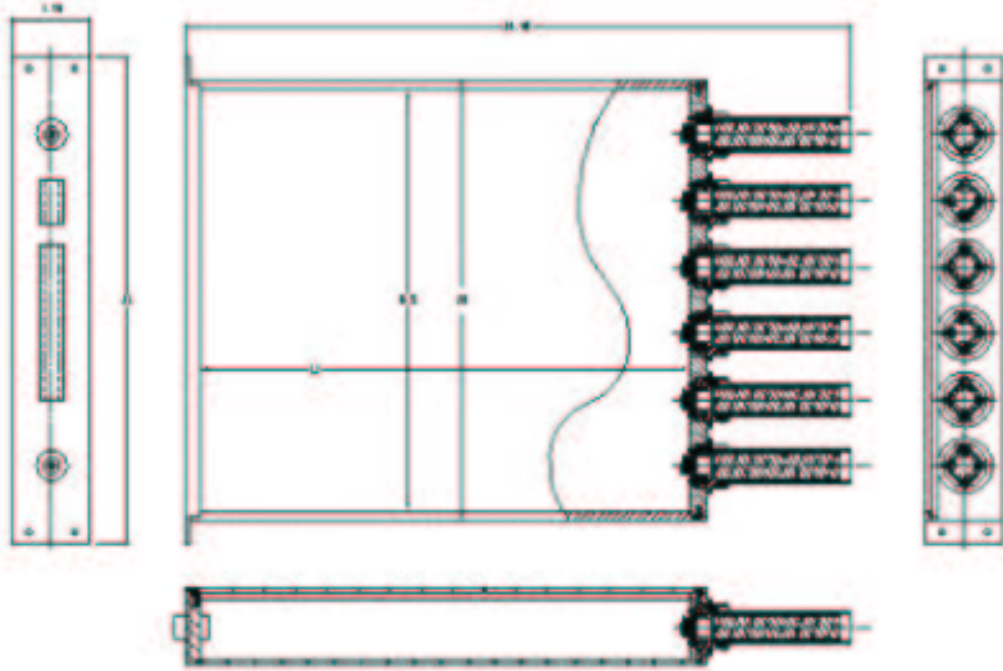


Fig. 32. The ICD electronics drawers

Fig. 33. The effect of ICD sampling on jet energy, as a function of detector pseudo-rapidity.

## 7 Muon system

The original DØ wide angle muon system (WAMUS) [8] and the new forward angle muon system (FAMUS) along with toroidal magnets, provide muon identification and measurement in the upgraded detector. The WAMUS system is composed of proportional drift tubes (PDTs) and provides coverage for  $|\eta| < 1.0$ . The new FAMUS detector uses planes of mini drift tubes rather than PDTs and extends muon detection to  $|\eta| = 2.0$ . The small angle muon system [8] of the original detector, along with its associated magnets, has been removed.

During Run I, a set of scintillation counters, the Cosmic Cap [29], was installed on the top and upper sides of the outer layer of WAMUS PDTs. This coverage has been extended to the lower sides and bottom of the detector, to form the Cosmic Bottom. These trigger scintillation counters are fast enough to allow us to associate a muon in a PDT with the appropriate bunch crossing and to reduce the cosmic ray coincidence.

Additional scintillation counters, the  $A\phi$  counters, have been installed on the WAMUS PDTs mounted between the calorimeter and the toroidal magnet. The  $A\phi$  counters provide a fast detector for triggering on and identifying muons and for rejecting out-of-time neutron background from the forward direction.

These detectors and the modifications made to the original system are discussed in detail in the following sections; original components are described briefly.

### 7.1 Toroidal magnets

The toroidal magnets are described in detail in Ref. [8]. The central toroid is a square annulus 109 cm thick whose inner surface is 317.5 cm from the Tevatron beamline; it covers the region  $|\eta| \lesssim 1.0$ . To allow access to the inner parts of the detector, it was constructed in three sections. The center-bottom section is a 150 cm wide beam, fixed to the detector platform, which provides a base for the calorimeters and tracking chambers. Two C-shaped sections, which can be moved perpendicularly to the center beam, complete the central toroid. The magnet is wound using twenty coils of ten turns each. The two end toroids are located at  $447 \leq |z| \leq 600$  cm. In the center of each magnet is a 183 cm square hole centered on the beamline; in  $x$  and  $y$  the magnets extend 417 cm from the beamline. The magnet windings are eight coils of eight turns each.



During Run I, the central and end toroids were operated in series at a current of 2500 A; the internal fields in the central magnet were approximately 1.9 T and those in the end magnets were approximately 2.0 T. During Run II, the magnets are again being operated in series, but at a current of 1500 A. The magnetic field is about 6% lower than that of Run I. Now, however, the primary measurement of the muon momentum is done by the new central tracking system and the reduced current provides a substantial cost savings. As in Run I, the polarity of the magnets is regularly reversed.

## 7.2 *Central muon detector*

The central muon system consists of toroidal magnets, the PDTs of the WAMUS system, the Cosmic Cap and Bottom scintillation counters, and the  $A\phi$  scintillation counters.

### 7.2.1 *WAMUS drift chambers*

The WAMUS drift chambers are described in detail in Ref. [8]. The three layers of drift chambers are located inside (A layer) and outside (B and C layers) of the central toroidal magnet. Approximately 55% of the central region is covered by three layers of PDTs; close to 90% is covered by at least two layers. The drift chambers are large, typically  $110'' \times 220''$ , and made of rectangular extruded aluminum tubes. The PDTs outside of the magnet have three decks of drift cells; the A layer has four decks with the exception of the A-layer bottom PDTs which have three decks. The cells are 10.1 cm across, with typically 24 cells per chamber. Along with an anode wire at the center of each cell, vernier cathode pads are located above and below the wires to provide information on the hit position along the wire.

For each hit, the following information is recorded: the drift time  $T$  to the anode wire, the difference  $\Delta T$  in the arrival time of the hit between a hit cell and the neighbor connected to it at the far end, and the charge deposition on the inner and outer vernier pads. Both  $\Delta T$  and the charge deposition are used to determine the hit position along the wire. The drift distance resolution is  $\approx 40 \mu\text{m}$ . The resolution of the  $\Delta T$  measurement varies depending on whether the muon passes through the cell close to or far from the electronics. If the hit occurs far from the electronics, the resolution is approximately 10 cm. If it is close, the signal propagates two wire lengths and the dispersion in the signal causes the resolution to degrade to about 50 cm. Using charge division, the pad signal resolution is about 5 mm. However, only the A-layer pads are fully instrumented; about 10% of the B- and C-layer pads are instrumented (??? distribution???)

To reduce the number of bunch crossings which occur during one drift interval, we are using a faster gas mixture than we used during Run I. The new mixture is 80% argon, 10% methane, and 10% CF<sub>4</sub>. The operating high voltage is approximately 2.5 kV for the pads and 5.0 kV for the wires. The drift velocity is thus  $\approx 10$  cm/ $\mu$ s, for a maximum drift time of  $\approx 500$  ns. The contribution to the hit position uncertainty due to diffusion is about 375  $\mu$ m, worse than the 300  $\mu$ m achieved using a slower gas during Run I. The poorer resolution is offset by the reduced occupancy and benefits to triggering due to decreasing the number of crossings in one drift time to two for 396 ns bunch spacing and four for 132 ns bunch spacing. The gas flow rate is  $\approx 500$  liters per hour (?????? – tdr says it will be 400-1000), a factor of five (??? 4-10 ???) higher than during Run I. The gas is recirculated and filtered in a cold trap to remove contaminants.

Vapors from a glue used in the construction of the cathode pads of the WAMUS drift chambers are deposited on the wires in a sheath whose thickness is proportional to the accumulated integrated charge. As the coating thickens, the gain of the chamber drops and the chamber becomes inefficient. This aging during Run II has been reduced by the increased gas flow, improved shielding, and by operating the chambers at a reduced gain. The aging cannot be prevented entirely and the chambers are cleaned as necessary. Since access to the A-layer chambers and the four central B-layer chambers directly under the detector is difficult, the cathode pads in these chambers have been replaced and no aging is anticipated.

calibration, more performance ???

The muon momentum resolution is  $\sigma(1/p) = 0.18(p - 2)/p^2 \otimes 0.005$  ( $p$  in GeV/ $c$ ) (??? still true??? Tom says probably). Figure 34 shows the momentum resolution of both the WAMUS system and the central tracking system which has a resolution of  $\delta p_T/p_T = 0.0015 p_T$  (???).

### 7.2.2 Cosmic Cap and Bottom counters

The Cosmic Cap and Bottom counters are installed on the top, sides and bottom of the outer layer of the WAMUS PDTs. They provide a fast timing signal to associate a muon in a PDT with the appropriate bunch crossing and discriminate against the cosmic ray background.

The Cosmic Cap counters are described in detail in Ref. [29]. They are made from grooved 0.5" Bicron 404a scintillator with BCF 91a and Kuraray Y11 wave-shifting fibers glued into the grooves using Bicron 600 optical epoxy. There are 240 counters, 0.5" thick, 25" wide, and 81.5"–113" long. The counters are positioned with their width along  $\eta$  and length along  $\phi$ . The grooves are 1.75 mm deep and 4 mm wide; they run along the length of the counter,

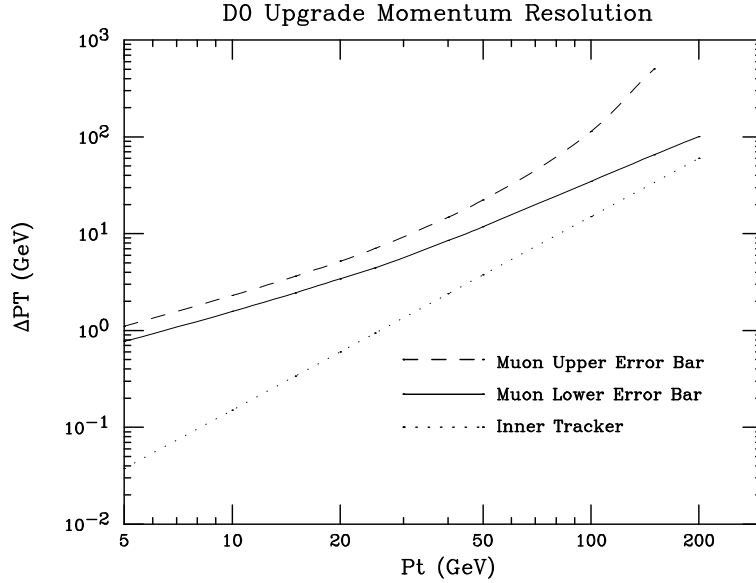


Fig. 34. Momentum resolutions of the central muon system and the central fiber tracker. The muon system resolution has separate upper and lower error bars because the uncertainty is in  $1/p$ . Note that the CFT resolution is always better than that of the WAMUS system.

from the end to just past the center. The grooves on each half of the counter are offset so they do not overlap at the center of the counter. They are spaced 8 mm apart so that half of the counter surface is covered with fibers. Each groove contains four fibers. The fibers are glued with five-minute epoxy at the ends of the counters which are then polished using a diamond cutter. To increase the light yield, a 1/32" anodized aluminum sheet is attached to the ends with aluminized mylar tape. The sides of the counters are milled. The fibers are gathered at the center of the counters, divided into two bundles with two fibers from each groove in one bundle and two in the other, and epoxied into two acrylic plastic cookies with holes in the center of each. The ends of the cookies are polished using the diamond cutter.

The scintillator is wrapped in a layer of Tyvek with a hole for the fibers and cookies; around the hole is an aluminum lip. A layer of 1/8" thick Styrofoam is placed over the fibers on the counter top; aluminum sheets 0.0020" thick cover the bottom and top surfaces. An outer frame of Unistrut provides support for the counter. A piece of black molded plastic fits over the outside of the aluminum lip and covers the phototubes, cookies and fibers.

The fibers are read out using two 1.5" 10-stage EMI 9902KA phototubes

mounted on the counters and operated in coincidence. The light yield varies depending on the distance from the phototube and the proximity to the edge. It is typically 30 photoelectrons per PMT for hits near the PMTs and 18 for hits near the distant corners.

The Cosmic Bottom counters complete the scintillator coverage of the toroidal magnet. There are 132 counters, of two different designs. The forty-eight counters located on the outside of the center bottom B layer of PDTs (where there is no C layer) are nearly identical to the Cosmic Cap counters described above. Some minor improvements were made in the placement of the edge fibers to increase the light yield and the counter frames are made from 1/8" steel bent into U-shaped channels. The counters are suspended from the strong edges of the PDTs.

The sixty-eight counters located on the undersides of the remaining B and C layers of the WAMUS PDTs are similar to the Cosmic Cap counters except that the Bottom counters have fewer fibers and they are placed in vertical, rather than horizontal, grooves. The grooves are approximately 6 mm deep and 6–10 cm apart. This distribution of fibers results in the same light yield as the horizontal arrangement used for the Cap counters. These counters use MELZ FEU-115 photomultiplier tubes which have a 1" diameter. They are 12-stage PMTs with a 2 ns risetime and good quantum efficiency and uniformity. The PMTs are placed within 42 mm diameter magnetic shields. Figure 35 shows a cut-away end view of a bottom B-layer counter including the scintillator and grooves, the PMTs and mounts, and the molded plastic cover and frame. The B-layer counters are suspended from the strong edges of the PDTs; the C-layer counters roll underneath the C-layer PDTs with one set of wheels in a track to maintain the counter position.

An important difference between the Cosmic Cap and Cosmic Bottom counters is that the Bottom counters are positioned with their narrow dimension along  $\phi$  and their long dimension along  $\eta$ . This orientation has better matching in  $\phi$  with the inner tracking chamber trigger. The counters' widths are approximately  $4.5^\circ$  in  $\phi$  and they are as long or slightly longer than their respective WAMUS PDTs are wide. Table 4 lists the location, number and size of the Cosmic Cap and Bottom counters.

??? Performance – in particular want a plot showing time distributions showing peaks from beam halo and backscatter. Like the one in the cosmic cap nim.

### 7.2.3 $A\phi$ scintillation counters

The  $A\phi$  scintillation counters cover the WAMUS A-layer PDTs, those between the calorimeter and the toroid. They provide a fast detector for triggering on and identifying muons and for rejecting out-of-time backscatter from the

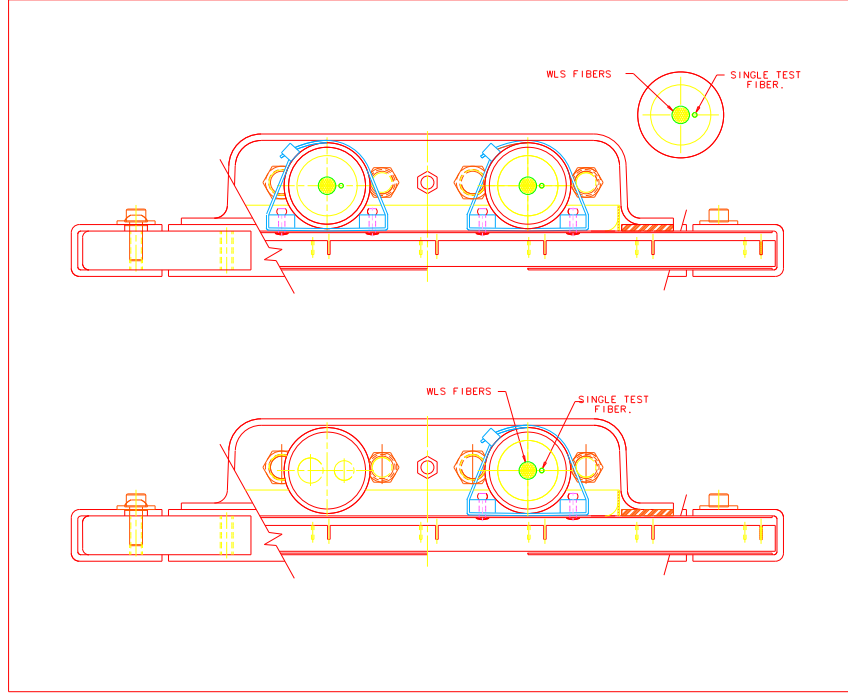


Fig. 35. Cosmic Bottom counter assembly. Notice that the grooves in the scintillator are oriented vertically.

forward direction. In-time scintillation counter hits are matched with tracks in the CFT in the Level 1 trigger (see Section 10.1) for unprescaled high- $p_T$  single muon and low- $p_T$  dimuon triggers. The counters also provide the time stamp for low- $p_T$  muons which do not penetrate the toroid and thus do not reach the Cosmic Cap or Bottom counters.

An end view of the  $A\phi$  counters is shown in Figure 36. The  $\phi$  segmentation is approximately  $4.5^\circ$  which matches the multiple scattering of high- $p_T$  muons. The longitudinal segmentation is 33.25" which provides the necessary time resolution and provides a good match to the size of the WAMUS PDTs; nine counters are required along the length of the detector. The nearly constant segmentation in  $\phi$  is accomplished through the use of three sizes of counter: 14.46", 10.84", and 9.09" wide. The widest counters are located at the corners of the detector, the narrowest at the center of each side. There is a gap at the bottom of the detector where the calorimeter support is located. The counters overlap an average of about 3% in  $\phi$  to reduce the possibility of muons passing through cracks. Along the length of the detector, the counters are butted end-to-end with a small gap between each.

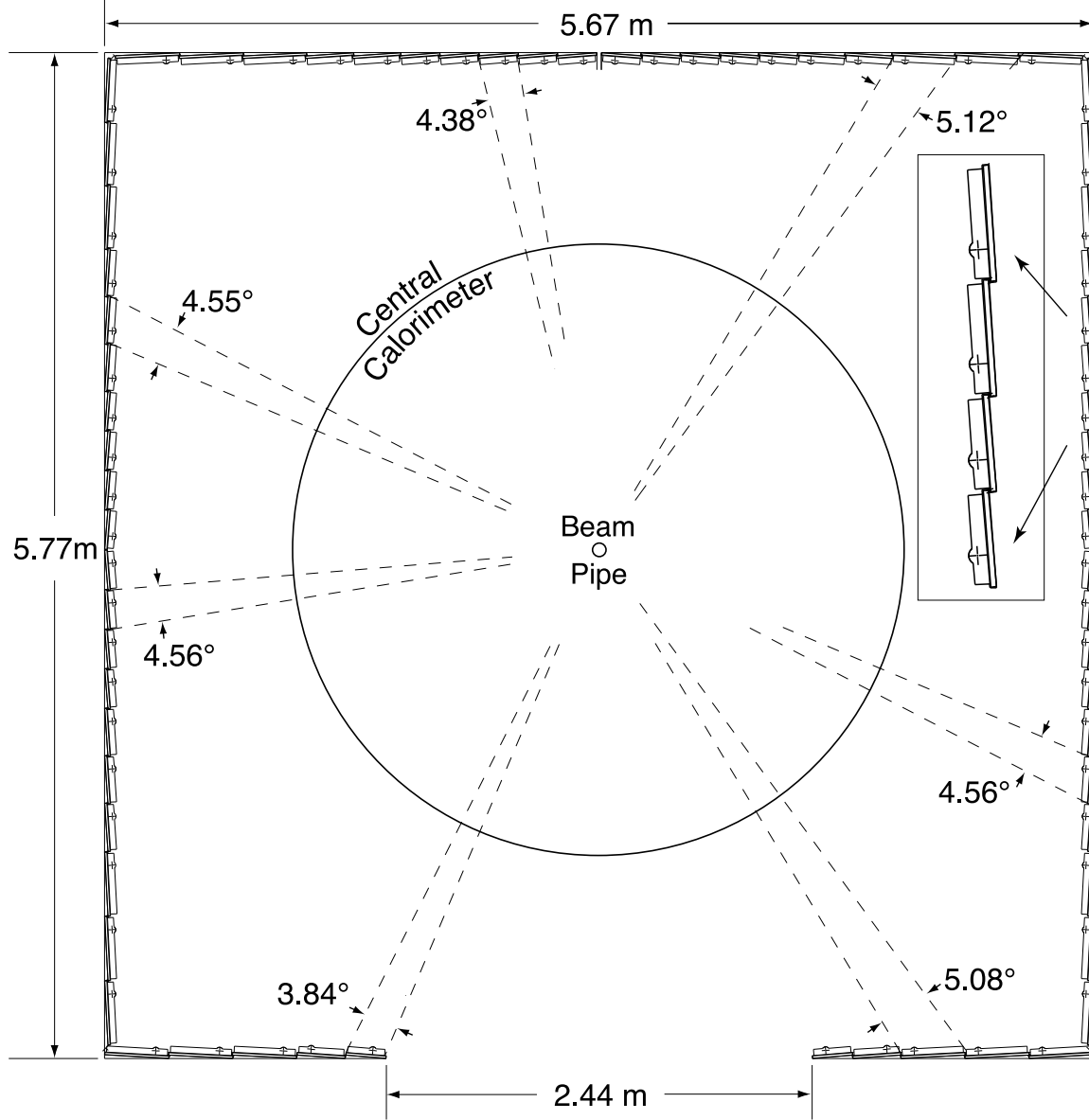


Fig. 36. End view of the layout of the  $A\phi$  scintillation counters. The inset box shows an enlarged view of four counters. Azimuthal coverage is shown for four of the counters. The bump on each counter represents the photomultiplier tube attached to the counter case.

The counters are made from Bicron 404a scintillator with G2 fiber embedded in vertical grooves in a manner similar to the Cosmic Bottom counters described above. The grooves are about 1.75" apart and run along the length of each counter from the edge to the middle. Six fibers are spot glued into each groove and taper out of the groove at the middle of the counter. The fibers are routed to a MELZ FEU-115 photomultiplier tube which is secured to the counter case. The counter and fibers are wrapped in a layer of TYVEK, followed by a layer of black TEDLAR. The counter case is an aluminum box with welded corners. It provides mechanical protection, support of the PMT and counter mounts,

and protection against light leaks. The counters are mounted on aluminum cross-members attached to steel brackets which are fastened to the edges of the WAMUS A-layer PDTs.

The counters operate in a magnetic field of 200–350 G due to the residual magnet fields of the toroidal and solenoidal magnets. Magnetic shields made of  $\mu$ -metal and soft iron with a diameter of 48 mm provide shielding from the component of the fringe field which is perpendicular to the PMTs; the maximum perpendicular field is about 250 G. A parallel magnetic field of 250(350) G causes a reduction in the gain of 5(10)%.

The performance of an  $A\phi$  prototype counter was studied using cosmic rays. The average counter signal corresponds to 50–60 photoelectrons. Comparison of the amplitudes of signals from the ends of the counters and from the center of the counter shows that the counters are uniform to  $\pm 7\%$ . The timing resolution of the counters is about 1 ns at a 20 mV threshold (???, read off of figure 17 in 3365, don't know what threshold is actually being used). The timing uncertainty is due to variation in the resolution of the counter (from the varying magnetic field and amplitude variation along the length of the counter), variation in the  $z$ -position of the vertex, variation in the  $z$ -position of the counter over its length, variation of the overall average time of collision of the bunches, and variation in the time of collision between bunches. Differing times-of-flight for particles at different polar angles are compensated for by varying cable lengths since the front-end electronics do not allow such timing adjustments.

Table 4

Location, number and size of Cosmic Cap and Bottom scintillation counters. All of the scintillator is 1/2" thick.

Location	Number	Width (inches)	Length (inches)	PMT
Cosmic Cap Top	80	25	113	EMI
Cosmic Cap Upper Sides	80	25	108	EMI
Cosmic Cap Lower Sides	80	25	81.5	EMI
Central Side B Layer	12	35	49	EMI
Central Side B Layer	4	35	67	EMI
Central Bottom B Layer	20	22 3/8	98 1/8	EMI
Central Bottom B Layer	20	15 3/4	98 1/8	EMI
Central Bottom B Layer Gap	8	18 1/2	99 1/2	EMI
End Bottom B Layer	20	13 3/8	91 1/16	MELZ
End Bottom B Layer	12	19 1/4	91 1/16	MELZ
Central Bottom C Layer	20	22 1/16	68 1/16	MELZ
Central Bottom C Layer	16	29 3/10	68 1/16	MELZ



Fig. 37. Design of the A layer of MDTs. The cutout at the bottom accommodates the calorimeter supports.

### 7.3 Forward angle muon system

The position of the FAMUS system is shown in Figure 1. It covers  $1.0 < |\eta| < 2.0$  and consists of four major parts: the end toroidal magnets, three layers of MDTs for muon track reconstruction, three layers of scintillation counters for triggering on events with muons, and shielding around the beam pipe.

#### 7.3.1 Mini drift tubes

Mini drift tubes were chosen for their short electron drift time (less than the 132 ns bunch crossing time), good coordinate resolution (less than 1 mm) and radiation hardness, and high segmentation and low occupancy. The MDTs are arranged in three layers (A, B, and C), each of which is divided into eight octants. A layer consists of three (layers B and C) or four (layer A) planes of tubes; eight  $1 \times 1 \text{ cm}^2$  cells comprise each tube. The layout of layer A is shown in Figure 37. The tubes are mounted along magnetic field lines (the field shape in the forward toroids is more “square” than “circular”). Each layer contains approximately 2000 tubes; the maximum tube length is 5830 mm in Layer C. Since the flux of particles drops with increasing distance from the beam line, the occupancy of individual tubes is the same within a factor of two over an entire layer.

A tube consists of eight cells, each with a  $9.4 \times 9.4 \text{ mm}^2$  internal cross section and a  $50 \text{ }\mu\text{m}$  W-Au anode wire in the center. The tubes are made from commercially available aluminum extrusion combs (0.6 mm thick) with a stainless steel foil cover (0.15 mm thick) and are inserted into plastic (PVC) sleeves. They are closed by endcaps that provide accurate positioning of the anode wires, wire tension, gas tightness, and electrical and gas connections. The anode wires are supported by 5 mm spacers; the unsupported wire length never exceeds 1 m.

The FAMUS system uses a  $\text{CF}_4\text{-CH}_4$  (90%-10%) gas mixture. It is non-flammable, fast, exhibits no radiation aging, and has a wide operational plateau. The maximum drift time for tracks which are perpendicular to the detector plane is 40 ns; for tracks inclined at  $45^\circ$ , the maximum drift time is 60 ns.

Negative high voltage is applied to the cathode ( $-3100 \text{ V}$ ); the anode wire is grounded at the amplifier. Each anode wire is connected to an amplifier and a discriminator located as close as possible to the signal connectors. Each amplifier discriminator board (ADB) contains 32 channels and detects signals with a threshold in the range  $0.5\text{--}5 \text{ }\mu\text{A}$ . Output logical differential signals from

Fig. 38. Detection efficiency of FAMUS MDTs.

the ADB are sent to digitizing electronics which measure the signal arrival time with respect to the beam crossing with an accuracy of 18.8 ns. This time bin limits the coordinate resolution of the MDTs. Hit information is sent to the trigger and data acquisition systems; the data acquisition system also receives drift times.

The efficiency of the MDTs is 100% in the active area of the cells for tracks which are perpendicular to the MDT plane. The overall efficiency is less because of the wall thickness, approximately 94% for our geometry. For inclined tracks, the walls are less important and the average efficiency approaches 100%. Figure 38 shows the efficiency for perpendicular tracks as measured in a test beam; the efficiency drops near the walls. The MDT efficiency is reduced near the wire-support spacers as well. Although each spacer is only 5 mm wide along the wire, the degradation in the electric field causes the efficiency to drop to approximately 20% for about 10 mm along the wire. Additional inefficiency is caused by the tube endcaps and gaps between octants for mounting, gas connections, and HV and signal cables.

To reconstruct a muon track segment, at least two hits (of the three or four possible) are required in a layer. Identification of soft muons which do not penetrate the toroid requires hits in at least three of the four planes of layer A. The two-out-of-three segment reconstruction efficiency is 99% while the three-out-of-four efficiency is about 98%.

The momentum resolution of the FAMUS spectrometer is limited by multiple scattering in the toroid and the coordinate resolution of the tracking detector. Although the MDT coordinate resolution measured in a test beam is about 350  $\mu\text{m}$ , the 18.8 ns time bin of the digitizing electronics leads to an overall track measurement resolution of about 0.7 mm per layer. The standalone momentum resolution of the FAMUS system is approximately 20%. The overall muon momentum resolution, including information from the silicon microstrip tracker and central fiber tracker, is defined by the central tracking system for muons with momentum up to 150 GeV/c; the FAMUS system improves the resolution slightly for higher momentum muons.

### 7.3.2 Trigger scintillation counters

The new muon trigger scintillation counters are mounted on the inside (layers A and C) or outside (layer B) of the FAMUS MDT planes. The design of the A layer of scintillation counters is shown in Figure 39. Each layer is divided into octants containing ninety-six counters. The  $\phi$  segmentation is  $4.5^\circ$  and matches the CFT trigger sectors. The  $\eta$  segmentation is 0.12 (0.07) for the first nine (last three) rows of counters. The largest counters, outer counters in

Fig. 39. Layout of the muon trigger scintillation counters for the A layer of the FAMUS system.

Fig. 40. Design of a scintillation counter for the forward muon trigger.

the C layer, are  $82 \times 48$  cm<sup>2</sup>. The B and C layers have geometries similar to that of the A layer, but limited in places by the collision hall ceiling and floor.

The counter design was optimized to provide good time resolution and uniformity for background rejection, high efficiency of muon detection, and reasonable cost for the production of nearly five thousand counters. A typical counter is shown in Figure 40. The counters are made of 0.5" Bicron 404A scintillator plate cut in a trapezoidal shape. Kumarin 30 WLS bars are attached to two sides of the plate for light collection. The bars are 4.2 mm thick and 0.5" wide and bent at 45° to transmit light to a 1" phototube. The phototubes are fast green-extended phototubes, 115M, from MELZ. They have a quantum efficiency of 15% at 500 nm and a gain of about  $10^6$ .

The sides of scintillator plates where the WLS bars are attached were left unpolished after milling. The unpolished sides give a larger number of photoelectrons and better uniformity than polished sides do (and cost less). The scintillator and WLS bars are wrapped in Tyvek material for better light collection and black paper for light tightness. The wrapped counters are placed in 1-mm-thick aluminum containers with stainless steel transition pieces for connection of the phototube assembly.

The fringe magnetic field due to the solenoid and the toroidal magnet reaches 350 G in the region where the phototubes for layer A are located. To reduce the field felt by the phototubes to approximately 1 G, they are placed in 48 mm diameter magnetic shields made of 1.2-mm-thick mu-metal and 3- or 6-mm-thick soft iron. Since the field near the A layer is larger, the shields there use 6 mm of iron. Those for the B and C layers use 3 mm. The effect of the magnetic field on the phototube signal is less than 10% for fields up to 350 G for the 6 mm thick shields.

The performance of three counters of different sizes was studied in a 125 GeV/ $c$  muon test beam. Figure 41 shows the dependence of the counter efficiency and time resolution as a function of high voltage for three counters: "large"  $60 \times 106$  cm<sup>2</sup>, "typical"  $24 \times 34$  cm<sup>2</sup>, and "small"  $17 \times 24$  cm<sup>2</sup>. The detection threshold for these measurements was set to 10 mV. The counter high voltage is set at 1.8 kV, which provides a time resolution better than 1 ns for all but the largest counters and a detection efficiency of 99.9%. The non-uniformity of the counter response was measured by irradiating counters at different points using a <sup>90</sup>Sr source and checked by cosmic ray studies. For all counters, the rms non-uniformity is less than 10%. Cosmic ray muons were used to deter-

Fig. 41. Time resolution and detection efficiency of muon trigger scintillation counters. See text for actual sizes.

mine the average number of photoelectrons detected in counters of various sizes. The largest counters have an average of 61 detected photoelectrons; the smallest counters give about three times as many photoelectrons.

Phototube signals are sent to 48-channel VME-based scintillator front end (SFE) cards. Input 1:1 transformers at the SFE card isolate the SFE from DC noise picked up between the phototubes and electronics modules which are located about 10 m apart. After amplification, the signals are sent to a 10-bit ADC and to a discriminator. Discriminated and gated signals are passed to the Level 1 trigger system and to the SFE TDC with a 1.0 ns time bin. After digitization, amplitude and time information is sent to the Level 2 trigger system and to the data acquisition system. The amplitude is measured in one out of sixteen channels per event for phototube gain monitoring. (??? added this from what Dmitri wrote)

The LED-based pulser system used to monitor the forward muon trigger scintillation counters is described in Section 7.4.

### 7.3.3 *Shielding*

Three sources contribute to non-muon background in the central and forward muon systems: scattered proton and antiproton fragments that interact with the end of the calorimeter or with the beampipe produce background in the central and forward A layer; proton and antiproton fragments interacting with the low-beta quadrupole magnets produce showers in the B and C layers of the FAMUS system; and beam halo interactions from the tunnel. Shielding installed in the accelerator tunnel during Run Ib significantly reduced the background from beam halo interactions. New shielding has been installed to reduce the background due to proton and antiproton remnants.

The shielding consists of layers of iron, polyethylene and lead in a steel structure surrounding the beam pipe and low beta quadrupole magnet. Iron is used as the hadron and electromagnetic absorber due to its relatively short interaction (16.8 cm) and radiation (1.76 cm) lengths and low cost. Polyethylene is a good absorber of slow neutrons due to its high hydrogen content. Lead is used to absorb gamma rays.

The position of the shielding is shown in Figure 1. It extends from the end calorimeter cryostat, through the end toroid magnet, to the end of the low beta quadrupole magnet. It consists of three rectangular cross section pieces that are 84", 85" and 60" long, starting at the toroid and moving forward. The piece closest to the toroid has a 20" square hole at the center followed by 16"

of iron, 6" of polyethylene, and 2" of lead. The two outer pieces are identical except that the hole is 25" square followed by 20" of lead. The most-forward section is split vertically down the center so that it can be moved out of the way when the end toroid magnet is opened.

Monte Carlo studies show that the shielding provides a factor of 50–100 reduction in the energy deposition in detector elements.

#### 7.4 *Muon scintillation counter monitoring*

The central and forward muon scintillation counters are calibrated and monitored using an LED-based pulser system. Given the large number of counters involved, it is not feasible to use cosmic ray and beam muons to check the timing and do the PMT gain calibration quickly. The LED system allows us to find dead PMTs, isolate the behavior of the PMTs from the front-end electronics, adjust the relative timing between channels, set initial PMT gains, monitor PMT gains, and track timing changes.

A pulser triggers an LED driver board that drives four LEDs embedded in an acrylic block. The light is further mixed in two additional Lucite mixing blocks. The upstream side of each block is frosted by sand-blasting; the sides of the blocks are polished to maximize total internal reflection. The light is then distributed to an array of clear optical fibers embedded in a fourth acrylic block. These light distribution fibers are connected to fibers which are butted up to each PMT. To match the peak wavelengths and emission spectra of the wavelength-shifting fibers used in the counters, different LEDs are used for the central and forward counters. In the central region, blue-green NSPE510S LEDs from Nichia America Corp. are used; in the forward region, blue NSPB320BS LEDs, also from Nichia America Corp., have been installed. The clear fibers are Hewlett Packard HFBR-500 optical fibers.

The light intensity of the LEDs is monitored using a PIN diode (Hamamatsu S6775) mounted at the downstream end of the first mixing block; this works because the mixing blocks evenly distribute the light to the fiber array. As long as the PIN diode is stable over time, variation in the gain of the PMTs can be measured independently of variation in the light output of the LEDs.

## 8 **Forward proton detector**

The Forward Proton Detector (FPD) [30] measures protons and antiprotons scattered at small angles (on the order of 1 mrad) that are missed by the bulk

of the DØ detector. During Run I, such diffractive events were tagged using a rapidity gap (the absence of particles in a region of the detector), however a forward particle detector is necessary for access to the full kinematics of the scattered particle. By detecting the scattered  $p$  or  $\bar{p}$  we can measure its momentum  $p$  and derive the variables:

$$x_p = p/p_{beam} \quad (1)$$

$$t = (p_{beam} - p)^2 \quad (2)$$

$$\xi = 1 - x_p \quad (3)$$

where  $t$  is the four-momentum transfer of the  $p$  (or  $\bar{p}$ ) and  $x_p$  is the fractional longitudinal momentum of the scattered particle.

### 8.1 The detector

The FPD consists of a series of momentum spectrometers that make use of accelerator magnets in conjunction with position detectors along the beam line. The position detectors operate a few millimeters away from the beam and have to be moved out during the injection of protons into the accelerator. Special stainless steel containers, called Roman pots [31], house the position detectors, allowing them to function outside of the accelerator's ultra high vacuum, but close to the beam. The scattered  $p$  or  $\bar{p}$  traverses a thin steel window at the entrance and exit of each pot. The pots are remotely controlled and can be moved close to the beam during stable conditions.

The Roman pots are housed in stainless steel chambers called castles. The FPD consists of eighteen Roman pots arranged in six castles. The castles are located at various distances from the DØ interaction point and in locations that do not interfere with any accelerator element. The experimental arrangement of the FPD is shown in Figure 42. Four castles are located downstream of the low beta quadrupole magnets on each side of the collision point: two on the  $p$  side (P1 and P2) and two on the  $\bar{p}$  side (A1 and A2). Each of these quadrupole castles contains four Roman pots arranged to cover most of the area around the beam. Two castles (D2 and D1) are located on the outgoing  $\bar{p}$  side after the dipole magnet. Each of these dipole castles contains only one Roman pot.

### 8.2 The position detector

Each position detector is made of 0.8 mm thick double-clad square scintillating fibers (Bicron BCF10 [32]) bundled in groups of four forming a scintillating

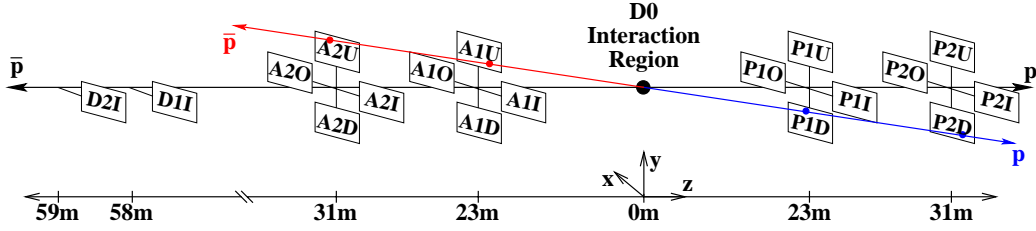


Fig. 42. FPD layout. Quadrupole castles are named P or A when placed on the  $p$  side or the  $\bar{p}$  side, respectively.

structure measuring  $0.8 \text{ mm} \times 3.2 \text{ mm}$ . One end of the detector element is aluminized (approximately  $3 \mu$  thick layer) to increase the light yield and the other end of each scintillating fiber is spliced to a double-clad clear fiber of square cross section (Bicron BCF98) with the same dimensions<sup>1</sup>. The scattered  $p$  or  $\bar{p}$  goes through  $3.2 \text{ mm}$  of scintillating material yielding approximately ten photoelectrons. The four clear fibers then take the light of one element to a single channel of the Hamamatsu H6568 16-channel multi anode photomultiplier (MAPMT). The use of clear fibers spliced to the scintillating fibers that constitute the active part of the detector reduces the effect of halo background in the fibers, the optical cross talk in the fibers, and minimizes light attenuation since clear fibers have an attenuation length longer than scintillating fibers.

Each detector consists of six planes in three views ( $u$ ,  $v$  and  $x$ ) in order to minimize ghost hit problems and to reduce reconstruction ambiguities. Each view is made of two planes ( $u - u'$ ,  $v - v'$  and  $x - x'$ ), the primed layers being offset by  $2/3$  of a fiber with respect to the unprimed layers. This arrangement yields a theoretical detector point resolution of  $80 \mu$ .  $u$  and  $v$  planes are oriented at  $\pm 45^\circ$  with respect to the horizontal bottom of the detector, while the  $x$  plane is at  $90^\circ$ . There are twenty channels in each layer of the  $u$  and  $c$  planes and sixteen channels in each of the  $x$  layers. There are 112 channels (each with four fibers) per detector giving a total of 2016 channels in the eighteen Roman pots. Each detector needs seven MAPMTs and includes a trigger scintillator read out by a fast photomultiplier tube (Phillips XP2282 [33]). Figure 43 shows the fiber arrangement and connection to the MAPMT. Figure 44 shows the FPD position detector. The FPD uses CFT electronics (described in Section 2.2.5) for the scintillating fiber detector read out, and luminosity monitor electronics (described in Section 9.1) for the trigger read out. The trigger manager designed for the muon system incorporates this information in making a Level 1 trigger decision on FPD tracks.

<sup>1</sup> The use of square fibers gives an increase of about 20% in light output compared to round fibers

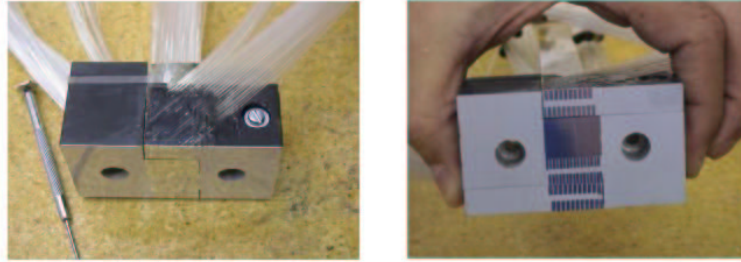
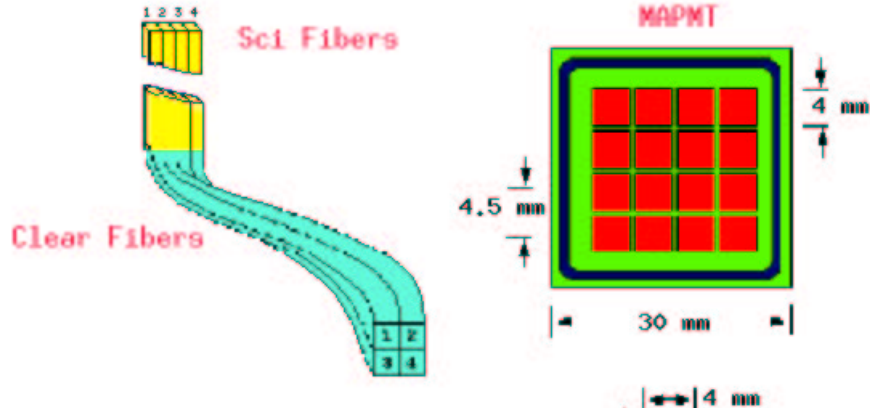


Fig. 44. FPD position detector.

### 8.3 The castle

Figure 45 shows the FPD castle. It has four arms, each containing a Roman pot housing a detector. The castles are made of 316L stainless steel and, due to the ultra high vacuum necessary in the interior of the castles, all parts were cleaned with demineralized water and alkaline detergent in an ultrasound bath and dried up with a hot air jet before being TIG welded. The castles can be baked at up to 150° C to improve the vacuum as necessary. A set of hot cathode and convection Pirani-style sensors monitors the vacuum in the chamber. Each castle has an associated ion pump to provide the ultra high vacuum.

Figure 46 shows the pot connected to the driving system that makes it possible to move the perpendicularly to the beam. A 200- $\mu$ -thick window separates



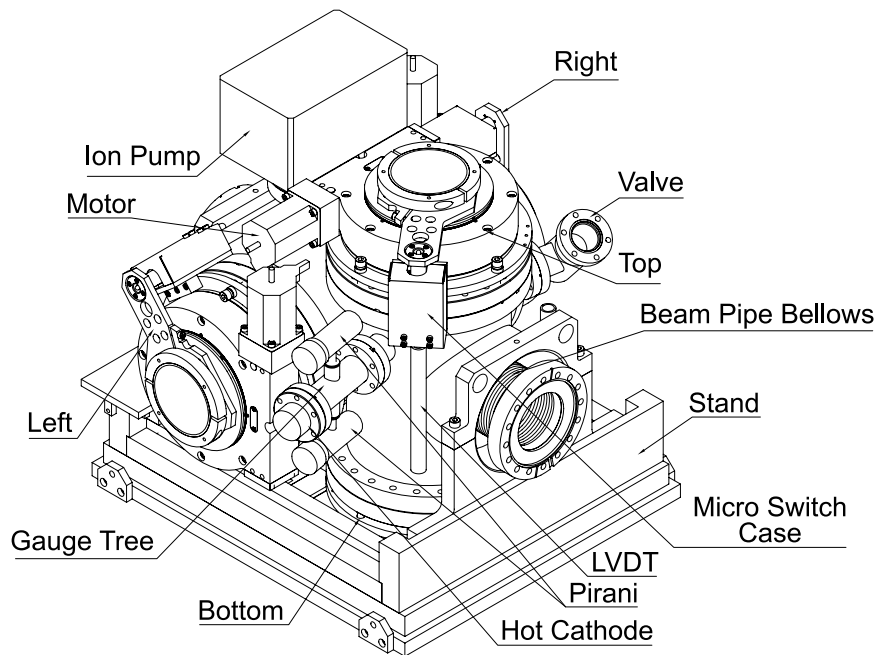


Fig. 45. FPD castle.

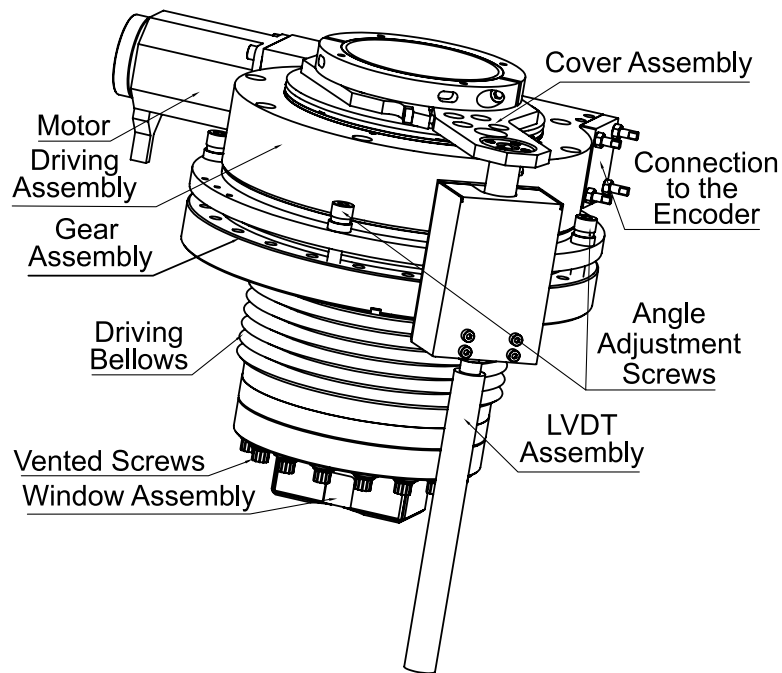


Fig. 46. FPD driving assembly.

the detector (inside the pot) from the castle ultra high vacuum. The system is operated by a step motor and a set of reduction gears allows pot motion with a precision of approximately  $5 \mu$ . A system of cylindrical and conical bearings allows adjustment of the pot alignment and a linear variable differential transducer (LVDT) monitors the pot position.

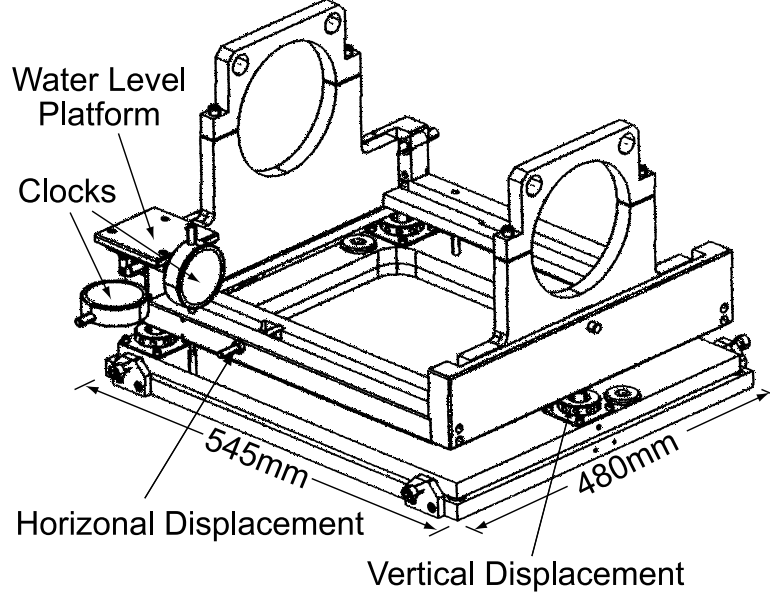


Fig. 47. FPD stand

To assure optimal alignment with the beam pipe and the positioning of the center of the castle vacuum chamber in the nominal position with respect to the center of the beam line, the castle sits on a stand shown in Figure 47. The stand consists primarily of a platform whose leveling is determined by three spindles. The stand allows the adjustment of the castle position in all directions over a range of 15 mm with an accuracy of 0.1 mm.

#### 8.4 Acceptances and resolutions

The FPD acceptance is maximized by minimizing the distance between the detectors and the beam axis. This distance is limited primarily by interaction with the beam halo which increase as the pots are inserted closer to the beam. The beam width,  $\sigma$ , is an important factor on determining how close to the beam the detectors can get without disturbing the accelerator performance. Figures 48 and 49 show the geometric acceptances for the dipole and the quadrupole detectors as functions of  $t$  and  $\xi$  calculated when the quadrupole pots are placed at a distance of  $8\sigma$  from the beam and when the dipole pots are placed at a distance of  $15\sigma$  from the beam.

For elastic events both particles must be detected by diagonally opposite spectrometers, as shown, for instance, in Figure 42, and no activity shall be detected in any other DØ subdetector. We collected a sample of elastic events during a commissioning run that was used to calculate  $\xi$  and  $t$  whose distributions are shown in Figures 50 and 51. We have also used this sample to measure the position resolution of the detector by using the  $u$  and  $v$  planes to measure the  $x$  coordinate and then compare it with the one given by the  $x$

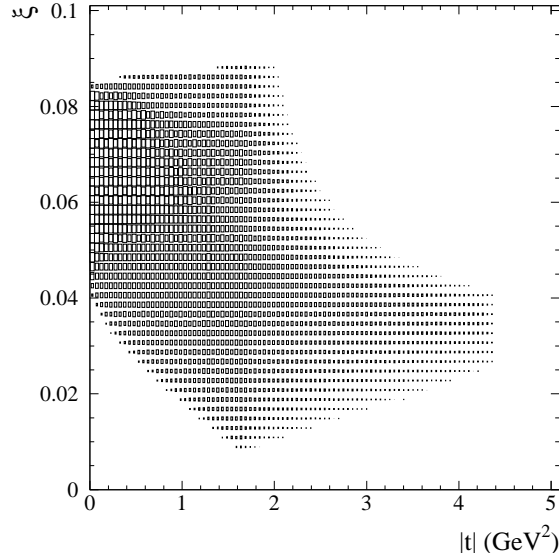


Fig. 48. Geometric acceptance in bins of  $\xi$  and  $|t|$  for the dipole spectrometer, with the detector at  $15\sigma$  displacement. The acceptance in each bin is proportional to the size of the box, with the largest box representing 100% acceptance.

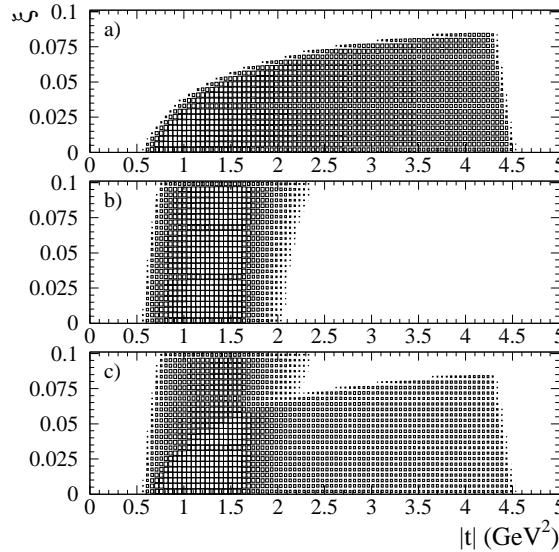


Fig. 49. Geometric acceptance for quadrupoles (proton side) at  $8\sigma$  displacement: (a) horizontal, (b) vertical, and (c) sum of both pots in bins of  $\xi$  and  $|t|$ . The size of the box is proportional to the value of the acceptance in that range of the parameters.

plane. This process gives a preliminary detector resolution of  $130\mu$ .

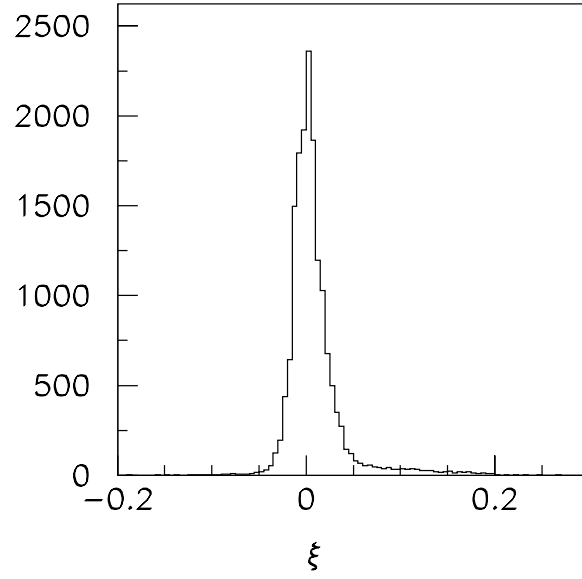


Fig. 50.  $\xi$  distribution

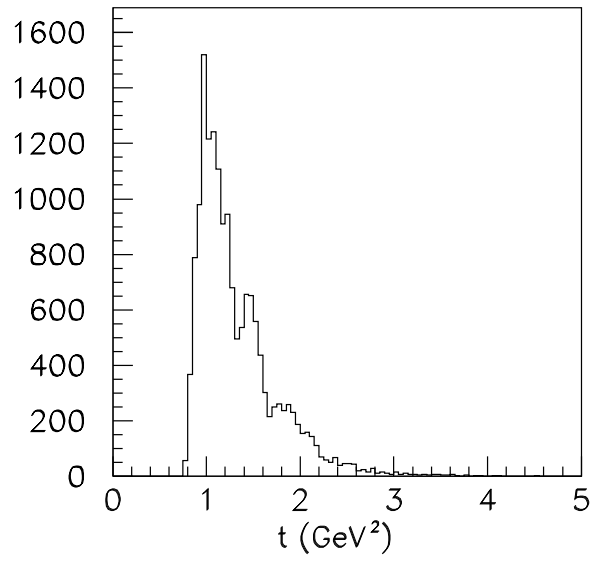


Fig. 51.  $t$  distribution

## 9 Luminosity Monitor

### 9.1 Readout electronics

## 10 Triggering and data acquisition

### 10.1 Triggering

### 10.2 Level 1 Muon Trigger

The Level 1 Muon Trigger (L1MU) looks for patterns consistent with muons using hits from muon wire chambers, muon scintillation counters, and tracks

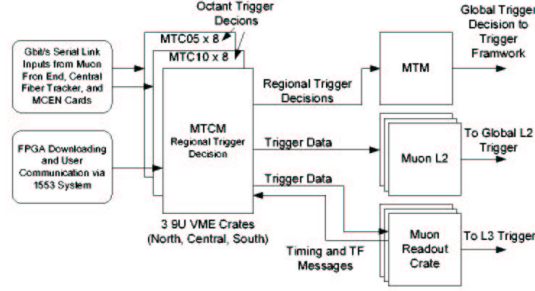


Fig. 52. Level 1 Muon Trigger system overview. Each octant has two trigger cards that process muon detector hit information and L1CTT tracks for that octant. The octant triggers for a given region are then summed on the MTCM and sent to the MTM, which combines the three regions and sends up to 32 triggers to the Trigger Framework.

from the Level 1 Central Track Trigger (L1CTT). Field Programmable Gate Arrays (FPGA's) are used to perform combinatorial logic on roughly 60,000 muon channels and up to 480 tracks from L1CTT for every bunch crossing. Data from the detector front-ends are transmitted on custom Gbit/s serial links over standard coaxial cable. The serial link receivers and FPGA's are located on VME cards that reside in four custom VME crates on the detector platform.

The muon system (and L1MU) is divided into a central, north, and south region. Each region is further divided into octants. Front-end data from each octant are processed by two L1MU trigger cards (Figure 52). The scintillator trigger cards (MTC05) match central tracks to muon scintillator hits while the wire trigger cards (MTC10) match scintillator-confirmed track stubs in wire chambers between the three layers of the muon system. The octant decisions from each MTC05/MTC10 pair in a region are summed in the Muon Trigger Crate Managers (MTCM's) and sent to a global trigger manager (MTM). The MTM forms 256 global L1MU triggers and sends up to 32 of these to the Trigger Framework for inclusion in the Level 1 physics trigger. The download of the specific triggers is handled via EPICS software.

### 10.2.1 Trigger Hardware

All detector inputs to L1MU use Gbit/s serial links, which transmit data over up to 150' of Times Microwave LMR-200 coaxial copper cable. The links are based on the AMCC S2042/S2043 fiber-optic transmitter/receiver pair and use an amplifier/equalizer circuit on the receiver to correct for the attenuation of the signal over the coaxial cable. The transmitters and receivers are 1.5"  $\times$  2.2" daughter cards that are mounted on the muon front ends and on the L1MU trigger cards. Each serial link can transmit up to  $16 \times 7 = 112$  bits every 132 ns bunch crossing. All MTC05, MTC10, and MTM trigger cards use

a common motherboard with sixteen serial links and different flavor daughter cards that perform the MTC05, MTC10, and MTM logic.

The MTC05 cards match tracks from L1CTT to hits in the muon scintillator system. Each octant trigger card receives tracks from the L1CTT for the ten  $4.5^\circ$  sectors in that octant plus one sector of overlap on either side. Each sector sends the six highest  $p_T$  tracks to L1MU, and each track contains the phi position in the outer layer,  $p_T$  value, and track curvature in the central magnetic field. The triggers formed by the MTC05 cards include loose (track matched to A-layer scintillator) and tight (track matched to a scintillator road using the A and B layers) for four  $p_T$  thresholds (roughly 1.5, 3, 5, and 10 GeV/c). Loose and tight scintillator-only triggers are also formed. The logic has been implemented on four 484-pin Altera ACEX 1K100 FPGA's and has a total latency of  $13 \times 18.8 \text{ ns} = 235 \text{ ns}$ .

The MTC10 cards form triggers based on wire hits. In the central region, the hits from the wire chambers (PDT's) are sent directly to the trigger cards. The hits for each layer are used to form track stubs, or centroids, which are then used to confirm scintillator hits in each layer. Triggers are formed by matching centroid-confirmed scintillator hits between layers. In the forward region, the centroid finding is done by separate centroid-finding cards (MCEN's), which subsequently send the centroids to the MTC10 cards. The MTC10 cards then uses the centroid-confirmed scintillator hits to form loose (A-layer) and tight (A and B-layer) triggers. The MTC10 logic has been implemented on seven Altera ACEX 1K FPGA's (three 1K100, three 1K50, and one 1K30). The latency in the central region is  $29 \times 18.8 \text{ ns} = 550 \text{ ns}$ , while in the forward region the latency is  $23 \times 18.8 \text{ ns} = 430 \text{ ns}$ .

The data from the various front end systems arrive asynchronously at L1MU and must be synchronized before triggers can be formed for a given event. To accomplish this, all received data are written directly into FIFO's which are initially empty. When all FIFO's are not empty (i.e., they have all received data for the first bunch crossing), the data are read from the FIFO's and sent to the MTC05, MTC10, or MTM flavor cards for trigger formation. In addition to synchronizing the data for a given event, the trigger cards also buffer the input data and trigger decisions pending global Level 1 and Level 2 trigger decisions. The input data and trigger decisions are stored in Dual Port Memories (DPM's) and a pointer to the data is written into a FIFO. When a Level 1 or Level 2 accept is received, the pointer is used to read the data for a particular event. The L1MU trigger can also send all of the received input data from the detector front-ends to aid debugging.

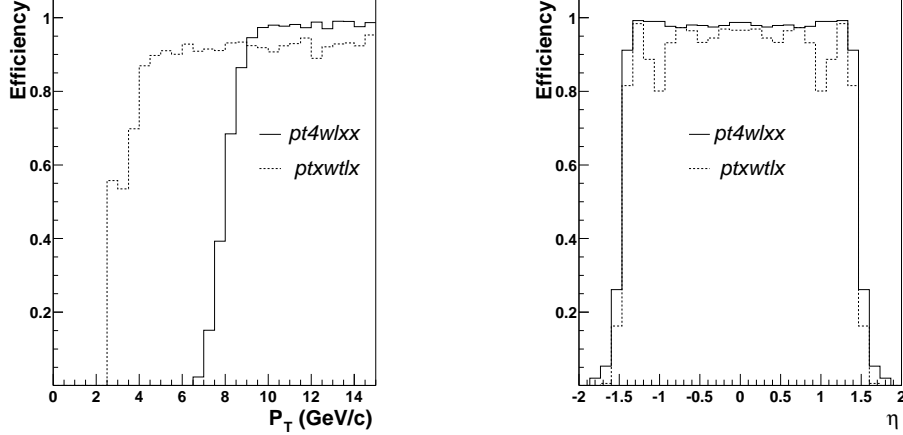


Fig. 53. The efficiency for the pt4wlxx trigger and the ptxwtlx trigger as a function of  $P_T$  and  $\eta$ .

### 10.3 Results

The L1MU trigger has been fully simulated in C++ as part of the DØ trigger simulator. The L1MU simulator (tsim\_l1muo) uses the digitized readout of the muon system and the results of the L1CTT simulator as inputs. Single muon Monte Carlo events are used to determine detector acceptance and trigger algorithm efficiencies. The L1MU simulator can also be run on collider data and the simulator results can be compared to the hardware L1MU trigger decisions. Presently this method of certification gives better than 1% agreement between the two. This simulator-hardware comparison is run online and used to monitor the performance of the L1MU trigger.

Results of the L1MU trigger simulator are given in Figure 53. The ptxwtlx trigger is a two-layer scintillator road and an A-layer wire centroid in the same octant, while the pt4wlxx trigger is a high- $P_T$  track matched to an A-layer scintillator hit. In these plots, the denominator is the number of Monte Carlo muons which have the minimum number of hits in the muon system to reconstruct a medium muon. The numerator is the number of events in the denominator that had a simulated trigger.

The total latency of the L1MU trigger is about  $3.20 \mu\text{s}$ , approximately 132 ns under the allowed  $3.35 \mu\text{s}$ . The latency is driven by the central wire chambers (PDT's) and tracks from L1CTT. The trigger rate at  $L=4\text{e}31 \text{ cm}^{-2}\text{s}^{-1}$  for the ptxwtlx trigger is about 450 Hz, while for the pt4wlxx trigger is about 400 Hz.

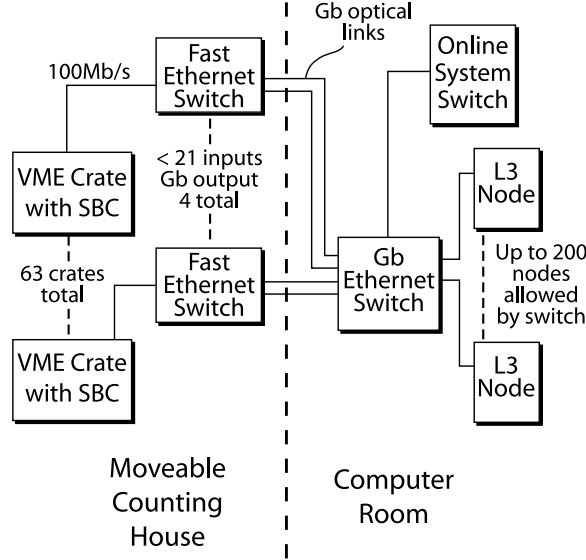


Fig. 54. The physical network configuration of the L3DAQ system.

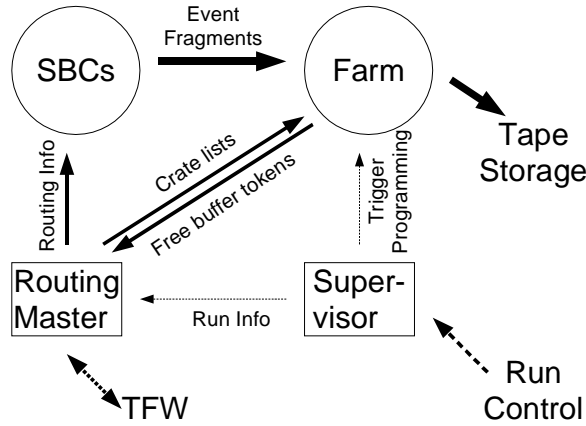


Fig. 55. Schematic illustration of the information and dataflow through the L3DAQ system.

#### 10.4 The Level 3 Data Acquisition System

The Level 3 Data Acquisition System (L3DAQ) transports detector component data located in VME readout crates to the processing nodes of the Level 3 trigger filtering farm. The system's designed bandwidth is 250 MB/s, corresponding to an average event size of 250 kB at a trigger accept rate of 1 kHz.

As shown in Figure 54, the system is built around a single Cisco 6509 [34] ethernet switch. A schematic of the communication and data flow in the system is shown in Figure 55. All nodes in the system are based on commodity computers and run the Linux operating system. TCP/IP sockets implemented via the ACE [35] C++ network and utility library are used for all communication and data transfers.



Sixty-three VME crates must be read out for each event, each containing 1–20 kB of data distributed among VME modules. A single-board computer (SBC) in each VME crate reads out the VME modules and sends the data to one or more farm nodes specified by routing instructions received from the Routing Master (RM) process. An Event Builder (EVB) process on each farm node builds a complete event from the event fragments and makes it available to Level 3 trigger filter processes.

The Supervisor process provides the interface between the main DØ run control (COOR) and the L3DAQ system. When a new run is configured, the Supervisor passes run and general trigger information to the RM and passes the COOR-provided L3 filter configuration to the IO/EVB process on relevant farm nodes, where it is cached and passed on to the Level 3 filter processes.

The SBCs are single-board computers with dual 100 Mb/s Ethernet interfaces and a VME-to-PCI interface. An expansion slot is occupied by a digital-I/O (DIO) module, used to coordinate the readout of VME modules over the VME user (J3) backplane. A custom kernel driver on the SBC handles interrupt requests from the DIO module which are triggered by readout requests from the crate-specific electronics. On each readout request the kernel module performs the VME data transfers and stores the event fragment in one of several buffers in kernel-memory.

A user-level process on the SBC receives route information from the Routing Master in the form of Route Tags that contain a unique event identifier (L3 transfer number) and the indices of the farm nodes to which that event should be sent. If the Route Tag's L3 transfer number matches that of the transfer number embedded within the head event fragment in the kernel buffers, the event fragment is sent to the specified farm nodes.

The Event Builder process on each farm node collates the event fragments received from SBCs into complete events, keyed by L3 transfer number. For each event the EVB receives an expected-crate list from the RM in order to determine when an event is complete. Complete events are placed in shared memory event buffers for processing by the Level 3 filter processes. The EVB routinely informs the RM of the number of available event buffers that it has. However, the EVB typically reports a much smaller number of free buffers (currently a maximum of three) than it has available, ensuring that the total number of events, and thus the total volume of data, flowing through the main ethernet switch at any moment is smaller than the size of the output buffer memory of the switch.

The Routing Master program executes on an SBC in a special VME crate which contains a hardware interface to the DØ trigger framework (TFW). The TFW provides trigger information and the L3 transfer number for each

event and allows the RM to asynchronously disable the firing of triggers. For each event the RM program chooses a node for processing based on the run configuration, the trigger information, and the number of available buffers in the set of nodes configured to process the type of event. A node is chosen in a round-robin fashion from amongst the set of nodes with the most free buffers. If the number of available free buffers is too few, the RM instructs the TFW to disable triggers so that the farm nodes have time to catch up.

#### *10.4.1 Online Host*

The online host system receives event data from the Level 3 farm nodes at a combined rate of approximately 12.5 MB/s (50 Hz L3 accept rate of 250 kB events) and distributes that data to logging and monitoring tasks. The host system is capable of supporting multiple simultaneous data runs. Events that pass the L3 filters are tagged with a data stream identification, which is a function of the satisfied hardware and software trigger components, with different streams recorded independently. Events are assigned to only one stream, excepting special monitoring streams.

The final repository for the raw event data is tape, maintained in a robotic tape system. Data must be transmitted to each tape drive at approximately 10 MB/s to keep the drive operating in streaming mode, since the tape drive nodes have no intermediate disk buffer. The system is capable of simultaneous output to multiple tape streams, and capable of buffering in case of tape robot unavailability. In addition to logging data, the host system must supply between ten and twenty data monitoring clients at anywhere from 1% to 100% of the full data rate.

Figures 56 and 57 illustrate the physical and software architecture of the online host system. Event data arrives from the Level 3 trigger nodes at Collector processes. The Collector directs each event to the Data Logger appropriate for the stream identifier determined for the event. The Collector also sends, on a best-effort basis (there is no flow control backpressure to the Level 3 nodes), a copy of each event to a Distributor process, which is an event queueing system that provides event data in near real-time to analysis and monitoring clients (EXAMINE programs).

An alternative diagnostic secondary data path, SDAQ, allows for processor-based readout of digitizing electronics. Information from SDAQ is also routed via the Collector mechanism, allowing all downstream DAQ components to be shared. This mechanism bypasses the L3DAQ and Level 3 trigger and is extremely valuable in the commissioning and calibration of detector components.

The Data Logger writes data to files, grouped according to stream classifi-

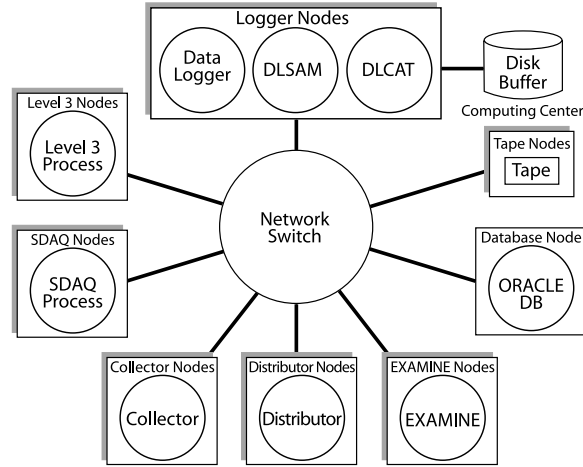


Fig. 56. Schematic of the physical architecture of the online host system.

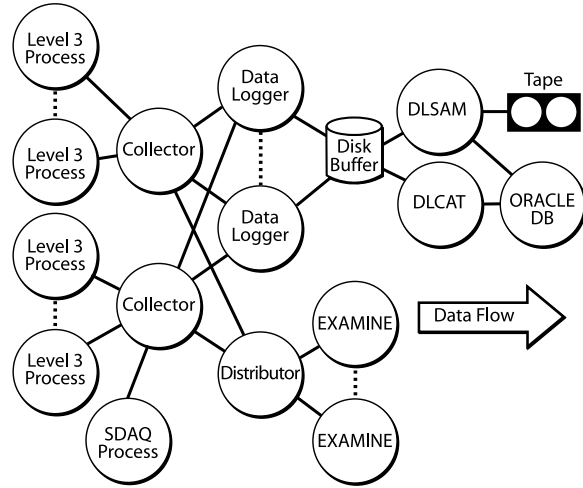


Fig. 57. Schematic of the software architecture of the online host system.

cation tags. Each Data Logger is responsible for a set of streams. The Data Logger also generates metadata information in file format for storage in a database to enhance the offline access of data. The DLSAM processes are the interfaces to the SAM/ENSTORE mass storage facility (see Section 12.5 and database system. DLSAM monitors the local data buffer disks and requests that files be stored in the mass storage system (ENSTORE). This request is made through the database interface (SAM) which negotiates the request for file storage with the ENSTORE system.

All of the online computing systems are connected to a single high-capacity network switch. The architecture provides for parallel operation of multiple instances of the bandwidth-critical components.

The high-level online software applications are predominately constructed using the Python scripting language. Network communication between the components is implemented with the ITC package, a multi-platform, multi-

threaded client/server messaging system based on the ACE [35] network and utility library.

## 11 Detector services

## 12 Computing and Software

A large amount of software has been developed for data acquisition, for monitoring and controlling hardware, for Monte Carlo event simulation, and for data and Monte Carlo event reconstruction. Early in the development of software for Run II, we made the decision that all new software would be written using the C++ programming language. Legacy Run I Fortran software and programs from other sources (e.g. Monte Carlo event simulation programs) are wrapped in C++ code. In this section, we give an overview of the computing and software used during Run II.

### *12.1 Event Data Model*

The DØ event data model (EDM) is a library of C++ classes and templates whose purpose is to support the implementation of reconstruction and analysis software.

The central feature of the EDM is the Event, a class that represents the results of a single beam crossing. The Event acts as a container to manage all the data associated with a single crossing: the raw output of the detector, the results of Level 3 filter processing, and the results of many different reconstruction tasks. Each of the items in this collection contains both the data describing the crossing in question as well as meta-data which describes the configuration of the program that constructed these results. This allows us to run multiple instances of single algorithms with different configuration information (for example, several cone-based jet algorithms with different cone radii), and to distinguish between the output of these different algorithms. The EDM also provides a mechanism for access to the collected reconstruction results, relieving the users from the burden on understanding the somewhat complex internal organization required for the management of the event data and the corresponding meta-data.

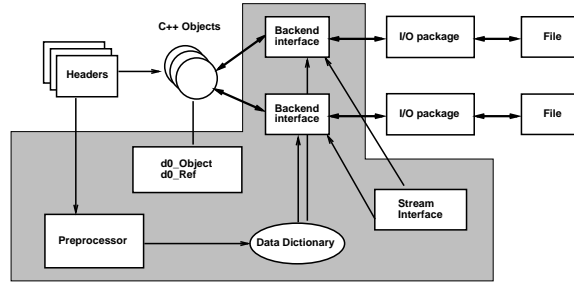


Fig. 58. The structure of DØOM. The shaded area shows the components which are a part of DØOM proper.

## 12.2 Data Persistency

The conversion of the C++ objects used in the reconstruction program to a persistent format is handled by the DØ object model (DØOM) [36]. This has several parts (Figure 12.2). First, DØOM maintains a dictionary describing the layout of the C++ classes that are to be used persistently, which is generated by running a preprocessor over the C++ headers defining the classes. This preprocessor is based on a modified version of the CINT C/C++ interpreter (which is also used in the ROOT system [37]).

The actual translation between C++ objects and the persistent format is handled by one of several I/O packages. User code has no dependence on the I/O packages, so that new formats can be added without changing any reconstruction code. The I/O packages are typically built on top of external software packages to do the actual I/O.

Finally, the external interface to the package is provided by a set of stream classes. A set of DØ framework packages that use these classes to read and write events within the framework are also provided; in most cases, a framework user need only to include these packages in order to read and write events.

DØOM includes numerous features to assist with schema evolution and versioning of data. The dictionary information is saved along with the saved data, so the layout of the saved data is always known. During reading, class members are matched between the C++ and persistent forms based on name. This allows DØOM to handle the common cases of adding and deleting data members with no explicit action on the programmer's part. For more complicated cases, it is possible to provide conversion code that is automatically run when needed. The DØOM dictionary information may also be queried at run time. The system can also make use of the persistent dictionary information to build objects at run time for which no dictionary information was compiled into the program. This is useful for programs to dump or browse arbitrary DØOM data files.

One I/O package is based on the DSPACK library, originally from the NA49 experiment [38]. DSPACK handles converting from C-like structures to a serial data format; the DØOM I/O package converts from the C++ objects to the DSPACK structures. At DØ, DSPACK data are usually encapsulated inside another, lightweight, format called EVPACK, which provides data compression and random access within files with keyed lookup. EVPACK-encapsulated DSPACK records may also be sent over the network; this is used to distribute data within the online host system. All event data are stored in (EVPACK-encapsulated) DSPACK format. In addition, this format is used for several static, structured data files used by the reconstruction program, such as the description of the detector geometry.

The other I/O package in active use at DØ is an interface to the commercial Oracle [39] database. C++ class definitions are automatically translated into an appropriate database schema. An interface is provided for making SQL queries to the database and retrieving the result as a collection of C++ objects. This package is used by the reconstruction program to access time-dependent configuration data, such as calibration constants.

### *12.3 Event Simulation*

The generation of Monte Carlo (MC) events involves multiple stages and many executables. To integrate all processes, all programs use the EDM to carry data in memory and the DØ object model (DØOM) to store persistent event data. All code is organized in independent packages running in a standard DØ framework and is written in C++ or embedded in C++ driving routines.

The first step in MC event generation is the simulation of a physical process, a  $p\bar{p}$  collision producing a particular final state. Nearly all existing event generator programs are written in Fortran, but the StdHep code from the FNAL Computing Division can be used to store the output in a standard common block format. This allowed us to write a C++ wrapper that converts the StdHep Fortran format to C++ classes satisfying the EDM requirements.

To trace the particles through the DØ detector, find where they intersect active areas, and simulate their energy deposition and secondary interactions, we use the CERN program GEANT v3.21, which is also written in Fortran. A C++ wrapper is used to read files produced by the event generators and to write the output of GEANT in DØOM format. This executable is called dØgstar. All subsequent steps in the event simulation are handled by programs written almost entirely in C++.

After the particles from the simulated reaction have been traced through the detector, the energy deposition must be converted to the form that the real

data takes when processed through the DØ electronics. Detector inefficiencies and noise (from the detector and electronic readout) must be taken into account, and more than one interaction may occur during a beam crossing. In addition, some portions of the detector (such as the calorimeter) remain sensitive to interactions over a period of time that includes more than one beam crossing. These effects are handled by the DØSim program. Simulation of the trigger electronics and the effects of the trigger on data selection is taken care of by a separate program, DØTrigSim. DØTrigSim contains simulation code only for the Level 1 trigger. The Level 2 and Level 3 triggers consist of filtering code running on processors specially designed for this purpose, and thus the same code running in the Level 2 and Level 3 processors runs in DØTrigSim. The output of DØSim and DØTrigSim is in the same format as the data recorded by the DØ data acquisition system, but contains additional MC information to make it possible to correlate detector information with the original generator information.

## 12.4 *Reconstruction*

The DØ offline reconstruction program (RECO) is responsible for reconstructing objects that are used to perform physics analysis. It is a CPU-intensive program that processes either collider events recorded during online data taking or simulated MC events. The executable is run on the offline production farms and the results are placed into the central data storage system for further analysis. Information and results for each event are organized using the EDM. The EDM manages information within the event in the form of chunks. The Raw Data Chunk (RDC), created either by the Level 3 trigger system or the MC, contains the raw detector signals and is the primary input to RECO. The output from RECO is many additional chunks associated with each type of reconstructed object. RECO produces two output formats or data tiers. The data summary tier (DST) contains all information necessary to perform any physics analysis, including limited re-reconstruction of high-level physics objects. The thumbnail (TMB) is a physics summary format less than one-tenth the size of the DST format. The TMB can be used directly to perform many analyses, and it allows the rapid development of event selection criteria to be applied to the DST sample.

RECO reconstructs events in several hierarchical steps. The first involves detector-specific processing. Detector unpackers process the RDC by unpacking individual detector data blocks. They decode the raw information, associate electronics channels with physical detector elements, and apply detector-specific calibration constants. For many of the detectors, this information is then used to reconstruct cluster (for example, from the calorimeter and preshower detectors) or hit (from the tracking detectors) objects. These ob-

jects use geometry constants to associate detector elements with physical positions in space. The second step in RECO focuses on the output of the tracking detectors. Hits in the SMT and CFT detectors are used to reconstruct global tracks. This is one of the most CPU-intensive activities of RECO, and involves running several algorithms. The results are stored in corresponding track chunks, which are used as input to the third step of RECO, vertexing. First, primary vertex candidates are found. These vertices indicate the locations of  $p\bar{p}$  interactions and are used in the calculation of various kinematical quantities (e.g. transverse energy). Next, displaced secondary vertex candidates are identified. Such vertices are associated with the decays of long-lived particles. The results of the above algorithms are stored in vertex chunks, and are then available for the final step of RECO — particle identification. Using a wide variety of algorithms, information from each of the preceding reconstruction steps is combined and standard physics object candidates are created. RECO first finds electron, photon, muon, neutrino ( $\cancel{E}_T$ ), and jet candidates. Candidates for heavy-quark and tau decays are identified next.

### *12.5 Data Handling and Storage*

The Sequential Access via Meta-data [40] (SAM) data handling system gives users access to all the files created by the DØ experiment (both detector data and simulation data), in a very flexible and transparent manner: the user does not need to know where the files are physically stored, nor worry about exactly how they are delivered to her/his process. SAM oversees the functions of cataloging data (files and events, and associated metadata regarding production conditions), transferring data in and out of mass storage systems, transferring data among different computer systems (whether connected via local or wide area network), allocating and monitoring computing resources (batch slots, tape mounts, network bandwidth, disk cache space), and keeping track at the user process level of file delivery status. The bookkeeping functions of the SAM system are handled by an Oracle [39] database, which is accessed via a client-server model utilizing CORBA technology. Files are stored in SAM using interfaces that require appropriate metadata for each file. The files are organized, according to the metadata provided, by data tier (RAW, DST, TMB), and by production information (program version which produces the data, etc.). The SAM system also provides file storage, file delivery, and file caching policies that permit the experiment to control and allocate the computing resources. Tape resources can be guaranteed to high priority activities (data acquisition and farm reconstruction), high usage files can be required to remain in the disk cache, and different priorities and allocations for resource usage can be granted to groups of users.



## Acknowledgements

## References

- [1] S. Abachi, et al., Phys. Rev. Lett. 74 (1995) 2632.
- [2] S. Abachi, et al. W mass references.
- [3] S. Abachi, et al. Gauge coupling references - lots, include all?
- [4] B. Abbott, et al., Phys. Rev. Lett. 79 (1997) 4321.
- [5] B. Abbott, et al., Phys. Rev. Lett. 80 (1998) 2051.
- [6] S. Abachi, et al. SUSY refs - lots here, too.
- [7] See <http://www.d0-www.fnal.gov/www.buffer/pub/publications.html> for a complete list of DØ publications.
- [8] S. Abachi, et al., Nucl. Instrum. Methods Phys. Res. A 338 (1994) 185.
- [9] R. Ruchti, Ann. Rev. Nucl. Part. Sci. 46 (1996) 281.
- [10] Kuraray International Corporation, 200 Park Ave., New York, NY 10166.
- [11] Reference for Noryl N190.
- [12] Reference for Celogen RA foam.
- [13] M. Petroff, M. Stapelbroek, IEEE Trans. Nucl. Sci. 36 (1989) 158.
- [14] M. Petroff, M. Atac, IEEE Trans. Nucl. Sci. 36 (1989) 163.
- [15] A. Bross, other, Nucl. Instrum. Methods Phys. Res. A 477 (2002) 172.
- [16] R. A. Rucinski, Short profile rectangular helium cryostat made from nickel-iron alloy, in: S. Breon, et al. (Eds.), Advances in Cryogenic Engineering, Vol. 46B, American Institute of Physics, Melville, New York, 2002, p. 1468.
- [17] CINCH Connector Division, A Division of Labinal Components & Systems, Inc., 1501 Morse Ave., Elk Grove Village, Il 60007.
- [18] Reference for Microchip.
- [19] B. Baumbaugh, et al., IEEE Trans. Nucl. Sci. 45 (1998) 343.
- [20] Need a reference for the calibration LEDs here.
- [21] F. Borcherdig, S. Grunendahl, M. Johnson, K. Yip, IEEE Trans. Nucl. Sci. 47 (2000) 381.
- [22] J. Olsen, et al., The dØ central track trigger, in: submitted to IEEE conference proceedings, 2003.

- [23] J. Brzenziak, et al., Fermilab-TM-1886 (1994).
- [24] Need a reference for Rutherford cable.
- [25] J. Simkin, C. Trowbridge, Three-Dimensional Computer Program (TOSCA) for Non-linear Electromagnetic Fields, RL-79-097 (1979).
- [26] A. M. Patwa, The forward preshower system and a study of the  $j/\psi$  trigger with the d0 detector (2002).  
URL  
[http://www-d0.fnal.gov/results/publications\\_talks/thesis/patwa/thesis.ps](http://www-d0.fnal.gov/results/publications_talks/thesis/patwa/thesis.ps)
- [27] NVF Company, P.O. Box 6069, Broadview, IL 60153.
- [28] Abatron Inc., 33 Center Dr., Gilberts, IL 60136.
- [29] B. Acharya, et al., Nucl. Instrum. Methods in Phys. Res. A 401 (1997) 45.
- [30] A. Brandt, et al., Fermilab-Pub-97/377 (1997).
- [31] U. Amaldi, et al., Phys. Lett. B43 (1973) 231.
- [32] [Www.bicron.com](http://www.bicron.com).
- [33] [Www.phillipsscientific.com](http://www.phillipsscientific.com).
- [34] [Www.cisco.com](http://www.cisco.com).
- [35] [Www.cs.wustl.edu/~schmidt/ACE.html](http://www.cs.wustl.edu/~schmidt/ACE.html).
- [36] S. Snyder, The d0 object model, presented at Computing in High Energy Physics '98, Chicago, <http://www.hep.net/chep98/PDF/130.pdf> (1998).
- [37] [Http://root.cern.ch/](http://root.cern.ch/).
- [38] R. Zybert, P. Buncic, Dspack: Object manager for high energy physics, Proceedings of Computing in High Energy Physics '95, Rio de Janeiro (1995) 345–348.
- [39] Need an ORACLE reference here.
- [40] A. Baranovski, et al., Fermilab-TM-2175 (2002).